

Effectiveness of the syndrome extraction circuit with flag qubits on IBM quantum hardware

Younghun Kim,^{1,*} Hansol Kim,^{1,†} Jeongsoo Kang,^{1,‡} Wonjae Choi,^{1,§} and Younghun Kwon^{1,¶}

¹*Department of Applied Physics, Hanyang University(ERICA), Ansan 15588, Republic of Korea*

Large-scale quantum circuits are required to exploit the advantages of quantum computers. Present-day quantum computers have become less reliable with increasing depths of quantum circuits. To overcome this limitation, quantum error-correction codes have been introduced. Although the success of quantum error correction codes has been announced in Google[1, 2] and neutral atom[3] quantum computers, there have been no reports on IBM quantum computers showing error suppression owing to its unique heavy-hexagon structure. This structure restricts connectivity, and quantum error-correction codes on IBM quantum computers require flag qubits. Here, we report the successful implementation of a syndrome extraction circuit with flag qubits on IBM quantum computers. Moreover, we demonstrate its effectiveness by considering the repetition code as a test code among the quantum error-correcting codes. Even though the data qubit is not adjacent to the syndrome qubit, logical error rates diminish exponentially as the distance of the repetition code increases from three to nine. Even when two flag qubits exist between the data and syndrome qubits, the logical error rates decrease as the distance increases similarly. This confirms the successful implementation of the syndrome extraction circuit with flag qubits on the IBM quantum computer.

All quantum computers currently consist of the noisy intermediate-scale quantum (NISQ) hardware[4]. Quantum computers cannot neglect the errors that occur when performing computations. Therefore, there is a need to implement a quantum error correction mechanism in quantum computers[5–11]. A fault-tolerant quantum computer can be constructed based on a quantum error-correcting code to get reliable results from arbitrary quantum circuits[12–14]. The IBM quantum machine, which has the largest number of qubits, has a heavy-hexagon structure rather than a lattice one. This is because the focus is on enhancing the performance of physical qubit gates in real quantum hardware, even if it means sacrificing hardware connectivity[15, 16]. Hence, implementing the quantum error correcting code in an IBM quantum machine may require flag qubits owing to its heavy-hexagon structure[17–23].

Previous studies have focused on evaluating the quantum error correcting code that does not have flag qubits in real devices such as the Sycamore device from Google, where physical qubits can have more connectivity when compared to the heavy-hexagon structure[1–3, 24–27]. In the case where flag qubits exist, quantum error correction in the current IBM machine has not been explored in terms of increasing the size of the structure[28–32]. However, in this study, we demonstrate that a syndrome extraction circuit with flag qubits in the repetition code can be successfully implemented on the IBM quantum machine.

As mentioned before, the IBM machine uses a heavy-hexagon structure, and it may require flag qubits to implement quantum error-correcting codes. Therefore, the effectiveness of the syndrome extraction circuit with flag qubits should be verified to determine whether the structure maintains error suppression. To verify the effectiveness of the syndrome extraction circuit with flag qubits, we select the repetition code, which is the simplest of surface code families. We test the performance of the syndrome extraction circuit with or without flag qubits on `ibm_kyoto`, an IBM quantum machine, by evaluating the machine’s efficiency in correcting errors. When there is a flag qubit in the syndrome extraction circuit, the data and syndrome qubits cannot be adjacent and interact directly. Therefore, we use the added flag qubits to connect the data qubits indirectly with the syndrome qubits[33, 34].

Fig. 1 illustrates how we detect an error that happens during the syndrome extraction circuits with initially selected physical qubits in the hardware. The error types considered are either bit-flips or phase-flips. When we verify the performance of the code on `ibm_kyoto`, the logical error rate of the repetition code containing the flag qubits decreases exponentially as the number of data qubits increases. This implies that the error correction can be performed using the syndrome extraction circuit with flag qubits in the repetition code on `ibm_kyoto`. More specifically, quantum error correction for bit-flips or phase-flips can be achieved on IBM devices, even when the data and syndrome qubits are not close.

Repetition code with flag qubits

A repetition code of distance d consists of a *one-dimensional* array of data qubits of $n_{data} = d$ and syndrome qubits of $n_{synd} = d - 1$. To consider a syndrome

*Electronic address: hpoqh@hanyang.ac.kr

†Electronic address: khshk18@hanyang.ac.kr

‡Electronic address: jskang1202@hanyang.ac.kr

§Electronic address: marchenw@hanyang.ac.kr

¶Electronic address: yyhkwon@hanyang.ac.kr

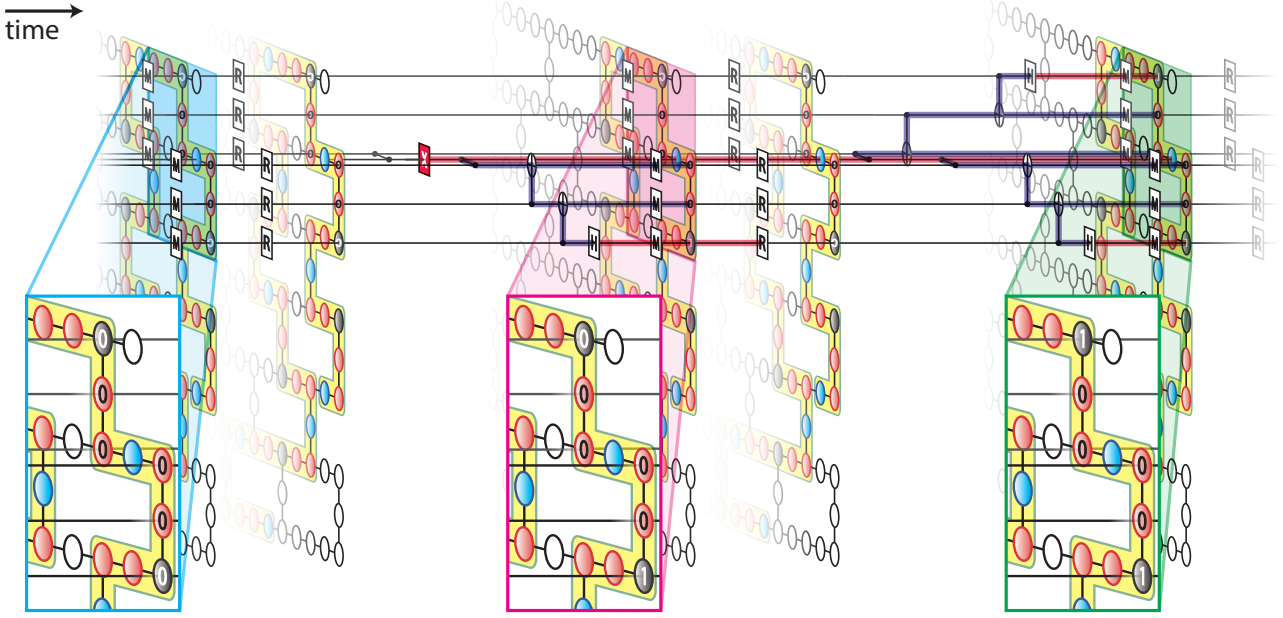


FIG. 1: Error detection in the repetition code using two flag qubits. The code uses initially selected physical qubits from a heavy-hexagon structure. The code progresses with time represented on the horizontal axis from left to right. The blue, black, and red dots correspond to data, syndrome, and flag qubits, respectively. The code undergoes multiple rounds of a syndrome extraction circuit, which involves reset and measurement gates on each syndrome and flag qubit. When the code uses the Z syndrome extraction circuit, we show the detection of an X error on a data qubit. The error is an example of an ST error. This error disseminates Z or X errors to nearby flag and syndrome qubits, indicated by the blue and red lines, from the data qubit. Over time, outcomes of three syndrome qubits, those closest to the data qubit, are affected: one is from the syndrome extraction circuit round highlighted with the magenta color, where the initial error occurs. The other two are from the subsequent round of the syndrome extraction circuit highlighted with the green color. The error can be detected by comparing consecutive measured outcomes of syndrome and flag qubits.

extraction circuit with flag qubits in the repetition code, a flag qubit needs to be added between the data and syndrome qubits to ensure they are not adjacent. If a single-flag qubit exists between them, the total number of flag qubits becomes $n_{flag} = 2n_{synd}$. However, when two flag qubits are used, the structure requires $n_{flag} = 4n_{synd}$ flag qubits. The repetition code can be denoted by $[n, k, d]_f$, where n and k are the numbers of data qubits and logical qubits, respectively, and d is the distance of the code. Notably, $f = 0$ implies no flag qubit; meanwhile, $f = 1$ and $f = 2$ denote single-flag qubit and double-flag qubits, respectively, between the data and syndrome qubits.

We can detect one type of error in a system using the defined stabilizer operators. The stabilizers are either Z or X stabilizers. The Z and X stabilizers are defined with operators from two adjacent data qubits. Therefore, the stabilizer is composed of i^{th} and $(i+1)^{th}$ data qubits' operators, where i belongs to $1, 2, \dots, d-1$. The Z stabilizer can only detect and rectify the X error. Meanwhile, the Z error can be detected and corrected using the X stabilizer. The Z and X stabilizers belong to

S_Z and S_X , respectively.

$$S_Z = \langle Z_i Z_{i+1} \rangle, S_X = \langle X_i X_{i+1} \rangle \quad (1)$$

The logical state of the repetition code can be defined using the stabilizers. The logical states are spanned in a code space C . For example, the code space of the logical states using the Z stabilizers becomes $C = \{|\psi\rangle, S_i|\psi\rangle = +|\psi\rangle, |\psi\rangle \in (\mathbb{C}^2)^{\otimes d}, S_i \in S_Z\}$. The logical states on the Z basis are denoted as $|0\rangle_L = |0\rangle_{data}^{\otimes d}$ and $|1\rangle_L = |1\rangle_{data}^{\otimes d}$. The logical states on the X basis satisfy $|+\rangle_L = \frac{1}{\sqrt{2}}(|0\rangle_L + |1\rangle_L)$ and $|-\rangle_L = \frac{1}{\sqrt{2}}(|0\rangle_L - |1\rangle_L)$. However, to check the error correction of X basis logical states, we consider X stabilizers. Hence, $|+\rangle_L$ and $|-\rangle_L$ should be defined as $|+\rangle_L = |+\rangle_{data}^{\otimes d}$ and $|-\rangle_L = |-\rangle_{data}^{\otimes d}$. For both cases, the logical Pauli gates are defined as $Z_L = \prod_{k=1}^d Z_k$ and $X_L = \prod_{k=1}^d X_k$ which change the state of a logical qubit without introducing errors and consist of only the Pauli operators of data qubits.

If i^{th} stabilizer (S_i) anti-commutes with an error of a data qubit (U_ϵ), the error in the data can be detected.

$$S_i U_\epsilon = -U_\epsilon S_i \quad (2)$$

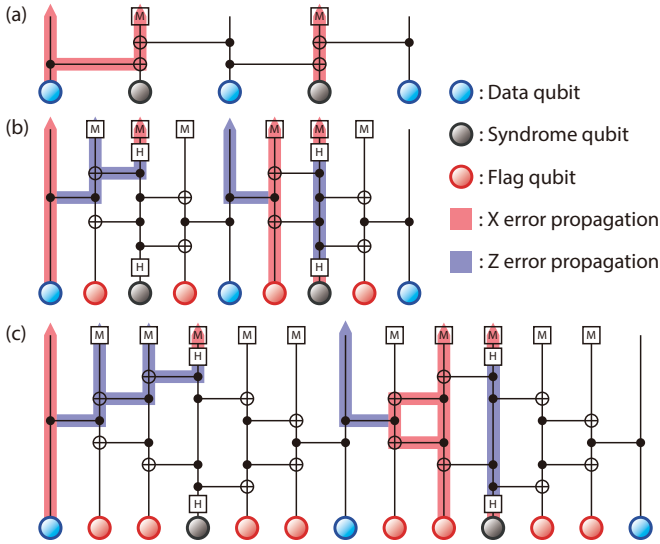


FIG. 2: Quantum circuit for the Z syndrome extraction circuit: (a) without a flag qubit, (b) with a single-flag qubit, and (c) with double-flag qubits. A syndrome qubit is prepared as $|+\rangle$ by applying the Hadamard gates and a flag qubit is prepared as $|0\rangle$. When a flag qubit exists, there is an indirect interaction between a data qubit and syndrome qubit via CZ and CNOT gates. The blue and red lines display propagated Z and X errors caused by the initialization error on one of physical qubits.

The error in the data qubit that anti-commutes with the stabilizer can be noticed by performing a subroutine quantum circuit, that is, a syndrome extraction circuit. Therefore, syndrome extraction circuits are used to detect the errors. Fig. 2 depicts the Z syndrome extraction circuits in the cases of no-flag qubit ($[3, 1, 3]_{f=0}$), a single-flag qubit ($[3, 1, 3]_{f=1}$), and double-flag qubits ($[3, 1, 3]_{f=2}$) between a data qubit and syndrome qubit. The X syndrome extraction circuits are listed in the supplementary material.

All data qubits interact with their neighboring syndrome qubits directly or through flag qubits to detect errors. Sequences of quantum operators are implemented to detect errors by measuring the flag and syndrome qubits. Above all, we explain a case in which there is no flag qubit. Every syndrome qubit is prepared as $|0\rangle$ to construct the Z syndrome extraction circuit depicted in Fig. 2 (a). To detect an X error in a data qubit, the CNOT operator is employed, with the data qubit serving as the control qubit and the syndrome qubit as the target qubit. The CNOT operations are performed in parallel to minimize the depth of the circuit. Fig. 2 (a) depicts how an error propagates in the circuit when an X error occurs in the data qubit on the left side. The bit-flip error propagates through the CNOT operator. Hence, the error affects its adjacent syndrome qubit.

Next, we explain the case in which there are flag qubits. When flag qubits exist, the data and syndrome

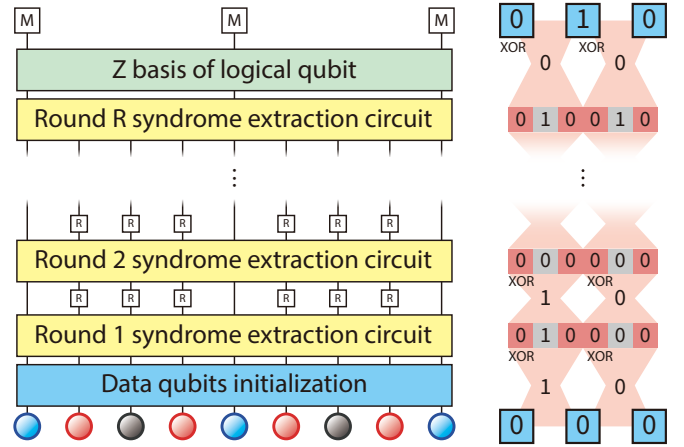


FIG. 3: Process example for syndrome extraction round in $[3, 1, 3]_{f=1}$. The figure explains the process of the quantum circuit that samples the result and calculates the syndrome from the measurement result. The quantum circuit consists of three parts: initializing data qubits, R rounds of the syndrome extraction circuit with reset gates on flag and syndrome qubits, and measuring data qubits. The outcomes from each stabilizer extraction circuit are used to obtain the syndrome by employing XOR gates across both temporal and spatial dimensions.

qubits cannot directly interact. If a single-flag qubit exists, as depicted in Fig. 2 (b), the error in the data qubit propagates to its neighbor syndrome qubit through the flag qubit. To detect errors, the structure is constructed as follows: The syndrome and flag qubits are initially prepared as $|0\rangle$. The Hadamard operators are applied to every syndrome qubit to change their states to $|+\rangle$. CNOT gates are implemented to create an entangled state for the syndrome and flag qubits. The CZ operator is applied between the data and the adjacent flag qubit. After applying CNOT gates in reverse order, we measure the syndrome and flag qubits on the Z basis. For the structure with a flag qubit between the data and syndrome qubits, when there is an X error in the data qubit, the error propagates to the flag qubit because the X error causes a Z error in the flag qubit through the CZ operator. The Z error cannot influence the flag qubit because the flag qubit is prepared as $|0\rangle$. Subsequently, the Z error, which propagates to the flag qubit, is transferred to the syndrome qubit through the CNOT operator and flips the syndrome qubit's outcome. Therefore, the X error in the data qubit can be detected by measuring the syndrome and flag qubits. For the structure with double-flag qubits in Fig. 2 (c), the data qubit error follows the same process, except being spread through another flag qubit next to the closest syndrome qubit.

In addition, errors are probable in syndrome or flag qubits. Here, let us consider an X error in initializing a syndrome qubit. The Hadamard gate is applied to

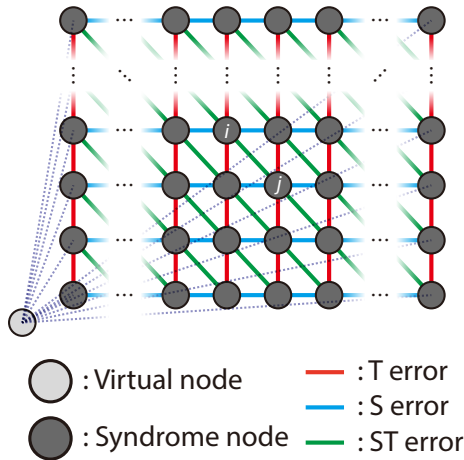


FIG. 4: Two-dimensional syndrome graph that displays a qubit error. Errors that are probable in the system are expressed as the S error (space error), T error (time error), and ST error (space-time error). The virtual node is introduced to show the S error on the boundary data qubits.

this error, and the error transforms into a Z error on the syndrome qubit. Because the syndrome qubit is a control qubit of the CNOT operators ahead of the error, the initial error is not propagated to flag qubits for the remaining gates. Therefore, although the error only produces a bit-flip in the measurement result of the syndrome qubit, it does not affect the quantum state of the data or flag qubits.

However, unlike syndrome qubits, errors in flag qubits may interact directly with data qubits. In Fig. 2 (b) and (c), when an X error occurs in the preparation of the initial quantum state of a flag qubit, the error undergoes two-qubit operators, which can be categorized as follows: 1. the CNOT operator between two flag qubits, 2. the CZ operator between a flag and data qubit. The first case produces an additional X error in another flag qubit. The CZ gate is applied to the propagated error. After the CZ gate, the propagated error is canceled when the initial error passes the second CNOT operator. In the second case, when the CZ gate is applied, the X error in the flag qubit propagates a Z error to the data qubit. However, the quantum state of the logical qubit is composed of data qubits on a Z basis and only considers X errors when the Z stabilizers are used. Therefore, the Z error in the data qubit may not change the computational state of the logical qubit, for which we are interested in whether the errors get corrected or not.

If the final quantum state of every data qubit can be corrected to its initial quantum state by a correction operator, the quantum correction code can be successful. Fig. 3 depicts the quantum memory experiment circuit with the Z syndrome extraction circuits to simulate and evaluate the performance of the code. To perform the single syndrome extraction circuit, the quantum state of

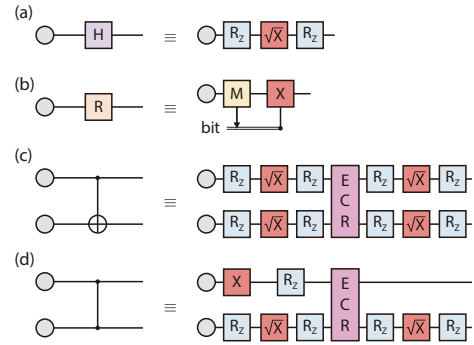


FIG. 5: Basis gate decomposition of `ibm_kyoto`. `ibm_kyoto` uses $\{R_Z, \sqrt{X}, X, \text{ECR}\}$ gate set as basis gates. The construction of logic gates of repetition code in terms of basis gates of `ibm_kyoto` are provided: (a) Hadamard gate, (b) conditional reset gate, (c) CNOT gate, and (d) CZ gate. Detailed information can be found in the supplementary material.

every syndrome and flag qubit should be initialized as $|0\rangle$. Hence, after each syndrome extraction circuit round, all the syndrome and flag qubits pass a reset gate. In the initial and final stages, the preparation of the initial state and the measurement of data qubits are performed on the Z basis. Therefore, $|+\rangle_L$ is prepared by preparing $|0\rangle_L$ and applying the Hadamard gate on all data qubits. The measurement at the final state can be obtained by measuring it on the Z basis. When the logical qubit is on the X basis, Hadamard gates are applied to the state before the measurement.

All measurement results of the syndrome and flag qubits can be listed in a sequence of bits. The binary measurement outcomes from two consecutive rounds pass the XOR gate and create n_{synd} syndrome bits. When syndrome extraction rounds are performed for N times, we can obtain $N - 1$ number of syndrome rounds between consecutive measurement rounds, which contains error information. Furthermore, we can build additional syndrome rounds based on the parity between data qubits and the results of the syndrome extraction rounds performed during the first and last times. Therefore, we obtain the results of $N+1$ syndrome rounds and the total $(N + 1) \times n_{synd}$ number of bit strings. When there is no error in the system, every syndrome and flag qubit is measured as $|0\rangle$, and all syndrome bits are obtained as 0. Hence, if the syndrome bit is 1, it indicates that an error has been detected, referred to as a defect syndrome.

Because we prioritize the effectiveness of a syndrome extraction circuit with flag qubits in the repetition code, we use the repetition codes with a distance of $\{3, 5, 7, 9\}$ and execute the syndrome extraction circuit 10 times with or without flag qubits. All quantum circuits are designed and run using the `qiskit` package[35]. Every case of $\{|0\rangle_L, |1\rangle_L, |+\rangle_L, |-\rangle_L\}$ is considered. In each round, we obtain 5×10^4 number of samples at each logical

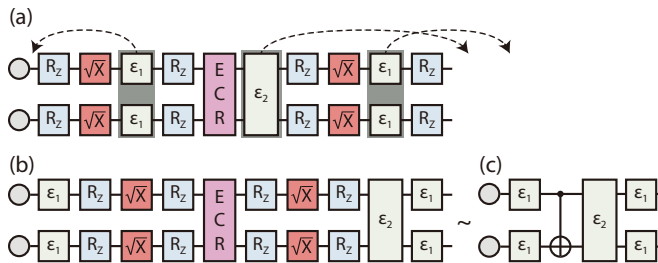


FIG. 6: Quantum circuit for the CNOT gate with quantum error channels. ϵ_1 and ϵ_2 denote the depolarizing error channels of single qubit and two qubits, respectively. (a) The CNOT gate can be constructed based on the gates of `ibm_kyoto` with depolarizing error channels. (b) The errors that occur during performing gates can be re-expressed as the error channels surrounding the CNOT gate. (c) The noisy CNOT gate can be fragmented into the error channels before and after the ideal CNOT gate.

quantum state, and the total number of samples is 2×10^5 . The experiment is conducted during each measurement round and initial state. Gate error rates can vary over time; therefore, we consider the error properties specific to each case for decoding and correcting errors. During the execution of a quantum circuit, dynamic decoupling sequences are added to all the data qubits during its idling period[36]. Moreover, we use a conditional reset gate to reduce the idling time of the data qubits in the syndrome extraction circuit[34].

Decoding by syndrome graph

We can infer the most probable correction operator by analyzing the syndromes obtained from the measurement results. A syndrome graph is constructed for this purpose. Fig. 4 depicts a two-dimensional syndrome graph in which the node denotes each bit of the syndrome in time and space, and the edges represent corresponding errors. Edges can be classified into T, S, and ST errors. The S(T) error denotes the error in the data qubit (syndrome or flag qubit), which produces a pair of defect syndromes in the corresponding nodes. The ST error denotes the case of consideration of an error that produces two defect syndromes diagonally such as an error of two-qubit gates on a data qubit, which can be seen in Fig. 1. A combination of these three types can express the errors in a system. The virtual node in the graph is employed to denote the error in the data qubit on the boundary (S error). Each edge has a weight calculated based on its error probability.

Once a syndrome graph is constructed, the decoding process follows: First, we extract the defect syndromes from the syndrome bit-string and map them onto the syndrome graph. Second, we build a defect syndrome graph by evaluating the weight of every edge constructed

by the defect syndrome nodes. The defect syndrome graph consists of syndrome nodes corresponding to the defect syndromes. Third, we find the pairs of defect syndromes by constructing a defect syndrome graph and applying a minimum weight perfect matching (MWPM) algorithm. Fourth, the most probable correction operator is obtained from the results of the MWPM algorithm[37, 38].

Two methods can be used to evaluate the weights of a syndrome graph. The first method exploits the error rates of every gate in the IBM hardware[21]. The second method uses the correlation between the results of the measured samples from the quantum circuit.

Hardware-based syndrome graph

The quantum memory experiment with the syndrome extraction circuit rounds of the repetition code consists of initialization, single qubit gates, CNOT gates, and measurements. However, the quantum hardware of `ibm_kyoto` uses $\{\text{ECR}, I, R_Z, \sqrt{X}, X, M\}$ as the basis gate. Notably, `ibm_kyoto` uses an echoed cross-resonance gate (ECR) for a two-qubit operator to create entanglement[41]. Therefore, quantum circuits should be expressed in terms of basis gates in the hardware. Fig. 5 shows that $\{H, R, \text{CNOT}, \text{CZ}\}$ can be expressed by combining gates in `ibm_kyoto`. Although the CNOT gate consists of eight R_Z , four \sqrt{X} , and a single ECR gate, the CZ gate can be fragmented into eight single qubit gates and an ECR gate. However, based on the parameters used for the R_Z gate, there are various methods to construct two-qubit gates, and a detailed explanation can be found in the supplementary material.

As explained previously, we can evaluate the weights of a syndrome graph using the error rates of every gate in the IBM hardware. The quantum circuit constructed with only Clifford gates can be simulated efficiently[39, 40]. Hence, an equivalent quantum circuit needs to contain a gate set with $\{\text{CNOT}, \text{CZ}, I, X, Z, H, M, R\}$ and an error channel with Pauli gates to obtain the weight of a syndrome graph[42]. Fig. 6 depicts the case for the noisy CNOT gate when there are quantum error channels such as ϵ_1 and ϵ_2 , which denote the depolarizing channels of the single-qubit and two-qubit gates. The error rate for both the single- and two-qubit gates can be adopted as the error rate from the corresponding gate in a real device. Because the depolarizing error channel and unitary gates are commutative, the noisy gates consist of the corresponding ideal gate and error channels. Since all basis gates except the R_Z are susceptible to errors[43], the depolarizing error channel is following after ECR, \sqrt{X} , and X gates. However, the readout and reset gate errors are considered with an X error instead of the depolarizing channel. While the noisy version for the other gates $\{\text{CZ}, I, X, H\}$ can also be constructed using depolarizing channels. We can design a quantum circuit by surrounding the ideal gate with depolarizing error

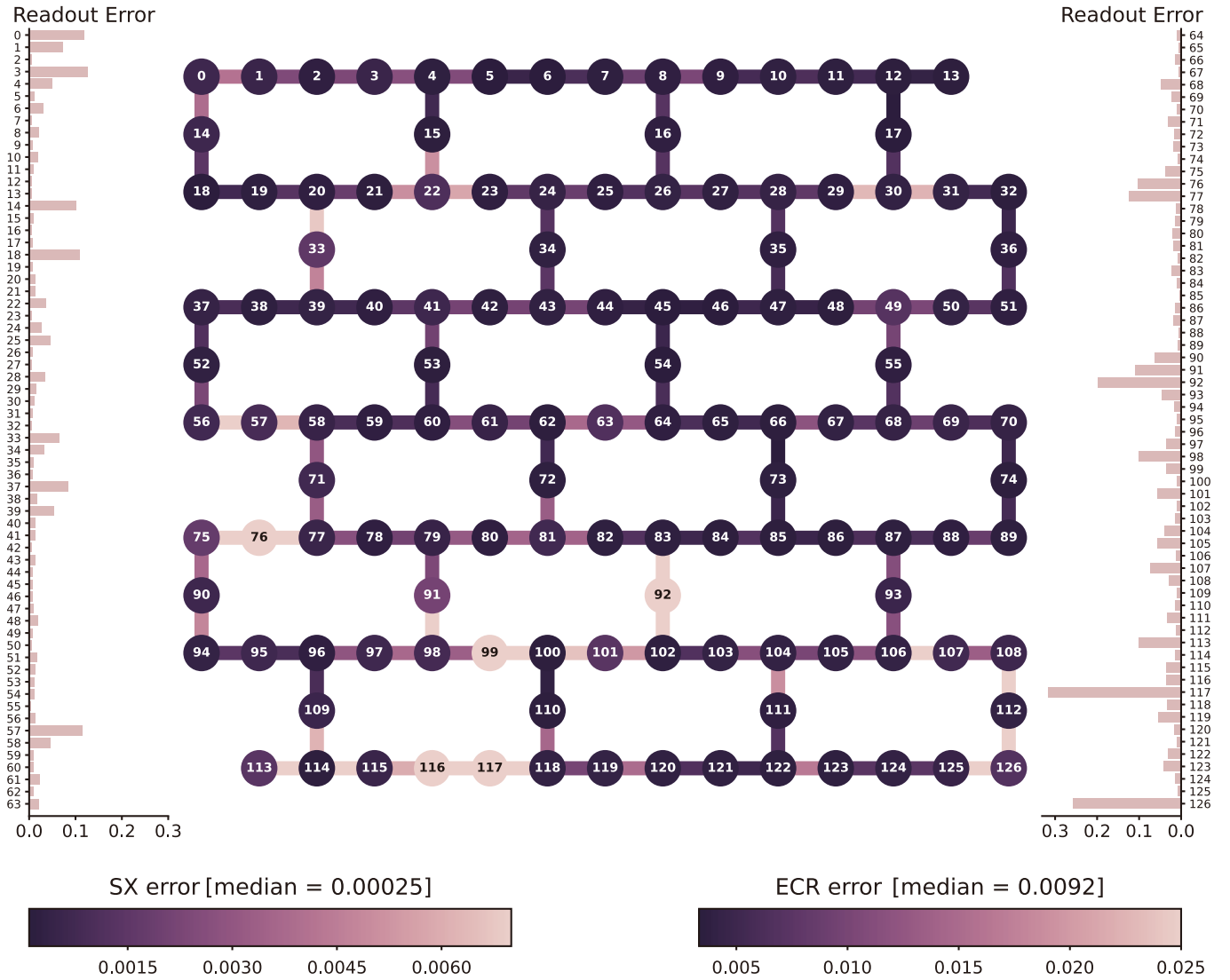


FIG. 7: Error rate of single qubit gate, ECR gate, and readout in 127 physical qubits of `ibm_kyoto` at 2023-12-25 11:42:34+00:00. While each readout error is displayed on the side, the error rate of the single-qubit and ECR gate are indicated using dots and edges, respectively, in the graph. The median error rate of the single qubit gate (ECR gate) is 2.5×10^{-4} (9.2×10^{-3})

channels, ensuring that the gate consists only of the Clifford gates. Therefore, we can construct a quantum circuit with Clifford gates, simultaneously considering the error rate of the hardware where its basis gates are not Clifford gates.

To implement a syndrome extraction circuit with flag qubits in the repetition code on `ibm_kyoto`, we select a combination of one-dimensional qubits from a heavy-hexagon structure of 127 qubits. Fig. 7 depicts the error rates of the SX gate, ECR gate, and measurement in `ibm_kyoto`[44]. The average of the lifetime (T_1) and coherence time (T_2) are $219.08 \mu\text{s}$ and $125.06 \mu\text{s}$, respectively. When a flag qubit is introduced between the data and syndrome qubits, we need 33 qubits in the case of $[9, 1, 9]_{f=1}$, because it uses 16 flag qubits between the data and syndrome qubits. If double-flag qubits exist

between the data and syndrome qubits, we need 49 qubits in the case of $[9, 1, 9]_{f=2}$, as depicted in Fig. 8 (a). Fig. 8 (b) shows that the ECR pulse, the measurement, and single qubit gate error rates in the selected qubits for the $[9, 1, 9]_{f=2}$ are expressed in terms of the empirical cumulative distribution function (ECDF).

Fig. 9 depicts the syndrome graph of $[9, 1, 9]_{f=2}$ obtained using the Stim code[42]. The weight for each edge in the syndrome graph can be determined by considering the probability of the corresponding error. We assign a lower weight when the probability is high, increasing the likelihood that the MWPM algorithm selects that error as a correction operator. The meaning of color is as follows: As the value of the weight increases, the intensity of the red color increases. Further, as the weight decreases, the intensity of the blue color

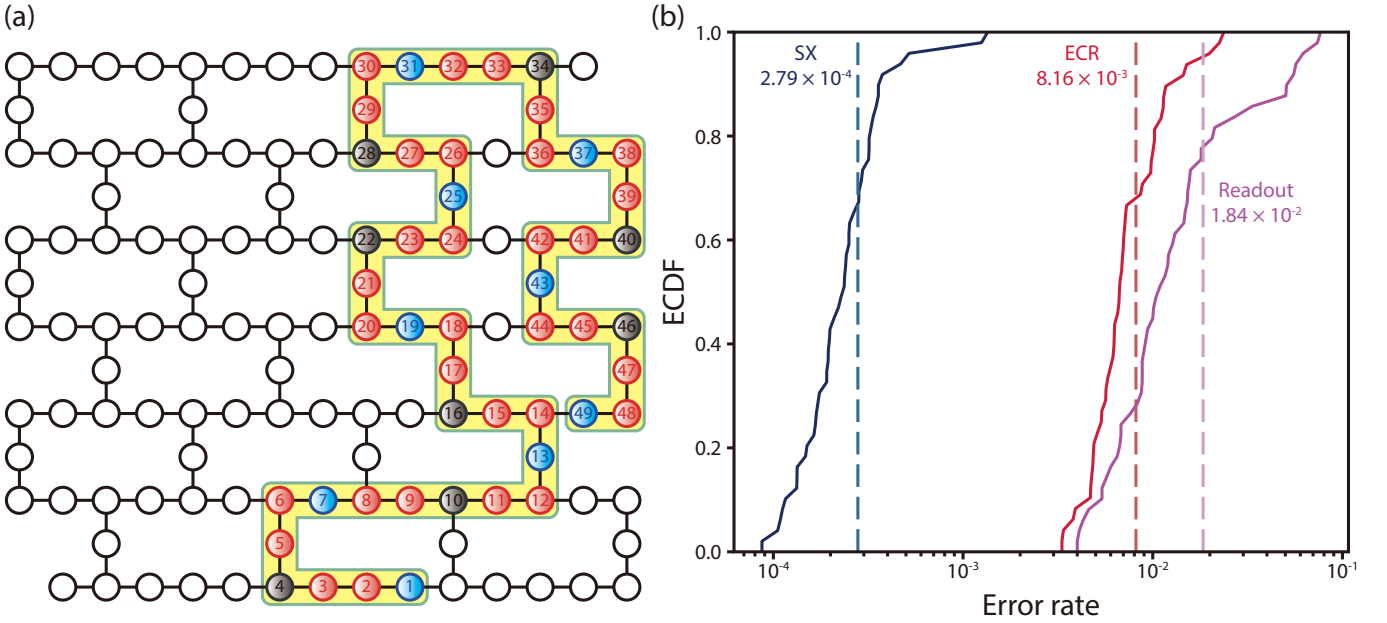


FIG. 8: The selected 49 physical qubits for $[9, 1, 9]_{f=2}$ and the error rate of `ibm_kyoto`. (a) The selected 49 physical qubits for $[9, 1, 9]_{f=2}$ are shown with color dots with respect to their types: data, syndrome, and flag qubits. The blue dots correspond to data qubits, black and red dots represent syndrome, and flag qubits, respectively. (b) The graph shows ECDF of gate errors for selected physical qubits at $[9, 1, 9]_{f=2}$. In this figure, error rates of quantum gates are considered when the initial logical state is $|0\rangle_L$. The cumulative distribution of each error of ECR, $SX(\sqrt{X})$, and readout are plotted as a function of the physical error rate. The dot lines correspond to their mean values.

Structure $[n, k, d]_f$	Error Type	Avg. weight
$[9, 1, 9]_{f=0}$	S error	5.560
	T error	4.387
	ST error	5.803
$[9, 1, 9]_{f=1}$	S error	5.260
	T error	2.893
	ST error	5.487
$[9, 1, 9]_{f=2}$	S error	4.874
	T error	2.038
	ST error	5.174

TABLE I: Average weights of S, T, and ST errors in the hardware-based syndrome graph when the number of data qubits is nine.

increases. This means the probability of selecting errors corresponding to edges indicated in blue increases.

Table 1 lists the average values of the weights for the cases of $[9, 1, 9]_{f=0}$, $[9, 1, 9]_{f=1}$, and $[9, 1, 9]_{f=2}$ with respect to the type of errors: S, T, and ST errors. As listed in Table 1, the weights corresponding to the measurement errors have smaller values regardless of the existence of the flag qubit. This tendency appears in the case of the average error rate of gates of `ibm_kyoto`. Furthermore, the weights with flag qubits have lower values than those without flag qubits. This implies that the more flag qubits we use, the more likely the errors occur.

Sample-based syndrome graph

The second method evaluates the statistical correlation between samples and uses it to decode errors[1, 2]. When p_{ij} is the probability where two syndrome nodes of i and j can be simultaneously defect syndromes, p_{ij} can be obtained by calculating the probability of defect syndromes on each node ($\langle x_j \rangle$, $\langle x_i \rangle$) or both simultaneously ($\langle x_i x_j \rangle$).

$$p_{ij} = \frac{1}{2} - \frac{1}{2} \sqrt{1 - \frac{4(\langle x_i x_j \rangle - \langle x_i \rangle \langle x_j \rangle)}{1 - 2\langle x_i \rangle - 2\langle x_j \rangle + 4\langle x_i x_j \rangle}} \quad (3)$$

If the error probability p_{ij} has a negative value, it is set to zero. The correlation matrix indicates the correlation between syndrome nodes. The number of syndrome nodes can be considered in terms of the horizontal direction corresponding to space and the vertical direction corresponding to time. The horizontal number is denoted by s , which can be $1, 2, \dots, d-1$. The vertical number is denoted by t , which can be $1, \dots, R+1$, where R is the number of rounds of syndrome extraction. The order of syndrome nodes can be determined in two cases: The first is when the priority is space, N_{s-t} , which is the space-time type. The second is when the priority is time, N_{t-s} , which is the time-space type. Syndrome

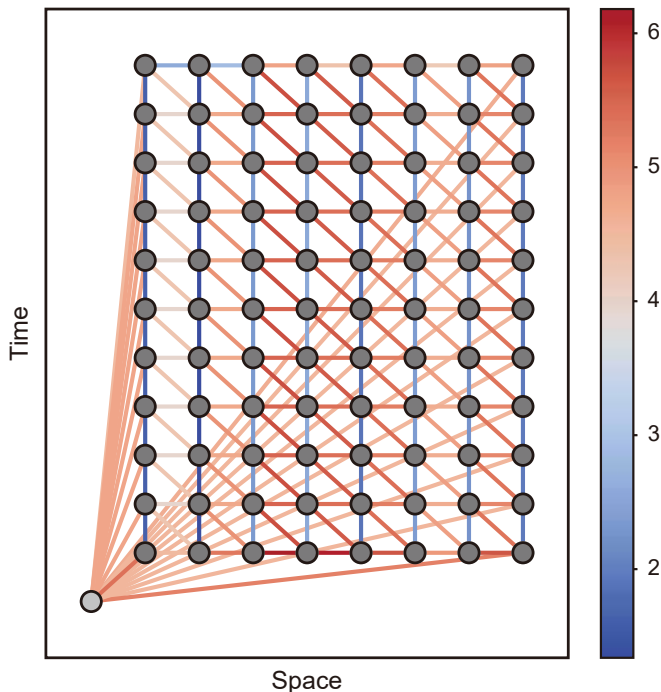


FIG. 9: Syndrome graph for a distance of 9 with double-flag qubits. The horizontal, vertical, and diagonal lines denote the S, T, and ST errors, respectively. The weight of each edge is obtained from the Stim code, which has the depolarizing error channel with the error rates of basis gates based on `ibm_kyoto`.

nodes can be labeled based on one of these methods.

$$\begin{aligned} N_{s-t} &= s + (d-1)(t-1) \\ N_{t-s} &= t + (R+1)(s-1) \end{aligned} \quad (4)$$

Fig. 10 (a), (b), and (c) depict the correlation matrix of syndrome samples of $[9, 1, 9]_{f=0}$, $[9, 1, 9]_{f=1}$, and $[9, 1, 9]_{f=2}$, respectively, which are displayed in terms of the forms of the space-time method. These figures exhibit the explicit correlation between syndrome nodes in space and time. The probability of detecting two defect syndrome nodes is higher in the presence of flag qubits than in their absence. As we add more flag qubits, we can see a higher probability of an error, which can be broken down into a combination of categorized errors (S, T, and ST error). This implies that the cross-talk effect becomes larger when flag qubits are included. T errors, caused by measurement errors on either syndrome or flag qubits, can occur consecutively over time because they are more frequent than S or ST errors. The phenomenon is observed in all cases, with or without flag qubits, as depicted in Fig. 10 (a), (b), and (c) with the dotted diagonal lines.

Table 2 lists the average weight of the syndrome graph obtained from the correlation matrix for the cases $[9, 1, 9]_{f=0}$, $[9, 1, 9]_{f=1}$, and $[9, 1, 9]_{f=2}$. When the weight is derived from the sampled data, time errors are

Structure $[n, k, d]_f$	Error Type	Avg. weight
$[9, 1, 9]_{f=0}$	S error	4.416
	T error	4.350
	ST error	5.533
$[9, 1, 9]_{f=1}$	S error	3.868
	T error	2.680
	ST error	5.101
$[9, 1, 9]_{f=2}$	S error	2.800
	T error	1.120
	ST error	4.321

TABLE II: Average weights of S, T, and ST errors in the sample-based syndrome graph when the number of data qubits is nine.

also more likely to occur, similar to the case with the hardware-based syndrome graph.

Fig. 11 (a), (b), and (c) depict the probability of the samples from the data concerning the number of defect syndromes according to the distance in the cases of no flag qubits, one flag qubit, and two flag qubits, respectively. The probabilities are evaluated by considering two logical qubit states, $|0\rangle_L$ and $|1\rangle_L$. The case in which the number of defect syndromes is zero implies that an error detected by the syndrome does not exist. In the case of $[3, 1, 3]_{f=0}$, the number of defect syndromes to be zero is 62.325% in the data, which implies that more than half become error-free. As a flag qubit is added, its probability of being zero decreases (23.904%), and the value is the lowest when double-flag qubits are added (0.322%) for distance three, which is the case of $[3, 1, 3]_{f=2}$. Further, the probability of the samples with an even number of defect syndromes is more significant than that for the number of cases to be odd, regardless of distance and the number of flag qubits. This is because only the S error located at the boundary can produce an odd number of defect syndromes. Notably, the probability of many defect syndromes in the presence of flag qubits is more significant than that without any flag qubits.

Logical error rate

Fig. 12 depicts the logical error rates in the hardware-based syndrome graph (a, b, c) and the sample-based syndrome graph (d, e, f) with different numbers of flag qubits. The experiment is performed according to the syndrome extraction round, and we obtain the average and standard deviation of the logical error rates for four different logical quantum states. The decoding results in the hardware-based and sample-based syndrome graphs exhibit similar behavior. The logical error rate is obtained by comparing the initially prepared logical quantum state with the corrected state. Logical errors can occur even when the number of defect syndromes is zero. Therefore, even when no defect syndrome is detected, we should check whether a logical error exists. When several defect

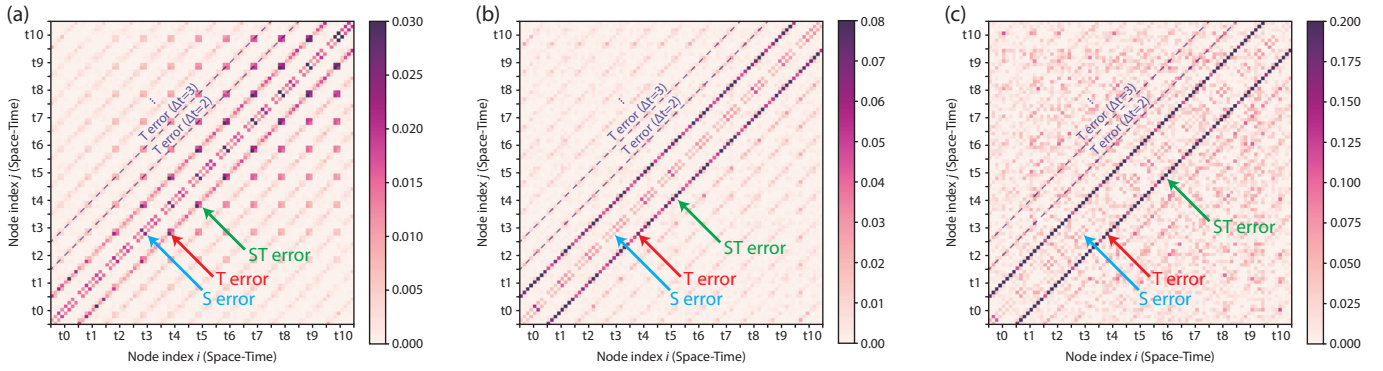


FIG. 10: Correlation matrices of repetition code at a distance of nine with different numbers of flag qubits. Space-time correlation matrices for (a) $[9, 1, 9]_{f=0}$, (b) $[9, 1, 9]_{f=1}$, and (c) $[9, 1, 9]_{f=2}$ are shown. The matrices are shown when the initial logical state is $|1\rangle_L$, and the number of rounds in the syndrome extraction is 10. Each pixel can be mapped on the edge of the corresponding syndrome graph. The S, T, and ST errors are visible along the diagonal line. The dashed diagonal lines correspond to multiple T errors occurring consecutively in a row. The axes represent the labeled syndrome node in the syndrome graph in the space-time method. Each syndrome round is divided as t , which varies from 0 to 10.

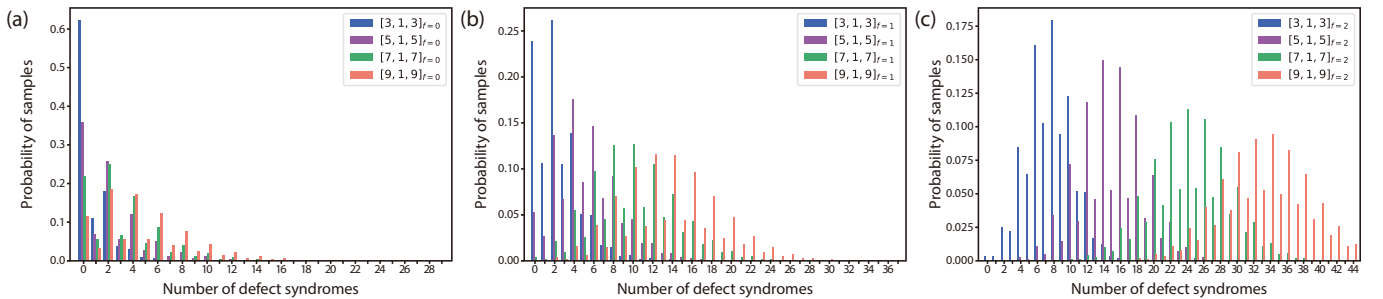


FIG. 11: Ratio between the number of corresponding sample and total number of sampled data in terms of the number of defect syndrome for (a) $[9, 1, 9]_{f=0}$, (b) $[9, 1, 9]_{f=1}$, and (c) $[9, 1, 9]_{f=2}$. The data is obtained with 10 rounds of syndrome extraction. The probability is calculated by considering Z basis states $|0\rangle_L$ and $|1\rangle_L$, meaning the total number of samples is 10^5 . The number of defect syndromes is plotted when its probability is more significant than 10^{-5} for all distances.

syndromes are detected, the Pymatching algorithm is used to decode given defect syndromes [37, 38]. Finally, by applying a correction operator to the measured data qubit, the updated data qubit state can be a logical qubit state. If the corrected state is different from the initial state, we count a failure.

Fig. 12 demonstrates the effectiveness of the syndrome extraction circuit with flag qubits in the repetition code on the IBM quantum machine. More specifically, in Fig. 12 we can see that in `ibm_kyoto`, the logical error rates of the repetition code exhibit an exponential decrease as the distance of the repetition code increases from three to nine. Even though the average gate error rates for each structure increase as we consider more flag qubits, this tendency remains when flag qubits are present, regardless of whether the syndrome graph is hardware-based or sample-data-based. This implies that even when the data qubit is not adjacent to the syndrome qubit, a repetition code can operate on the IBM quantum computer. Moreover, even when there exist double-

flag qubits between the data and syndrome qubits, a repetition code may operate on `ibm_kyoto`.

Conclusion

In this study, we showed the effectiveness of a syndrome extraction circuit with flag qubits in the repetition code on the IBM quantum machine, `ibm_kyoto`. The quantum error correction using a repetition code with flag qubits was realized in the IBM quantum machine, `ibm_kyoto`. Because the IBM machine uses a heavy-hexagon structure, in which the maximum connection of a single node is three, the use of flag qubits may be required. We demonstrated that even when two flag qubits exist between a data qubit and a syndrome qubit, the logical error rates diminish exponentially as the distance between the repetition code increases from three to nine. This implies that a syndrome extraction circuit with flag qubits remains

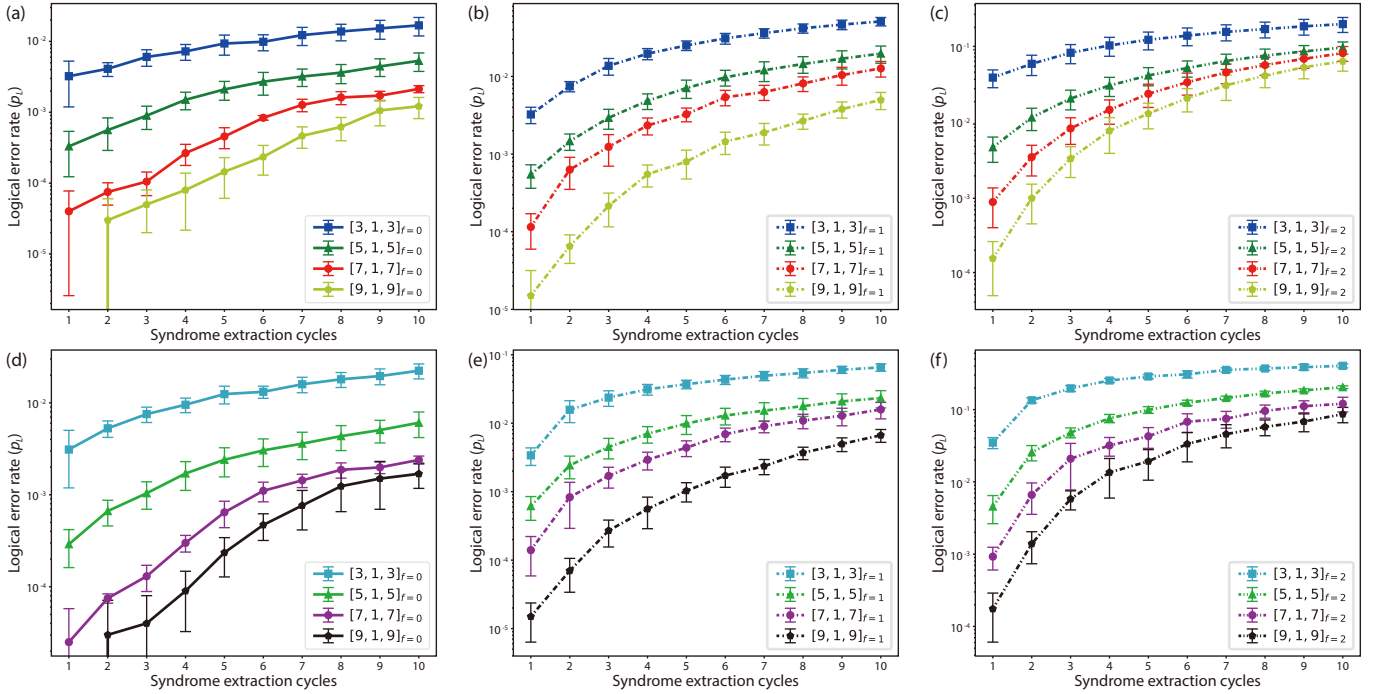


FIG. 12: Logical error rate of repetition codes. The figure displays the logical error rates of $[d, 1, d]_{f=0}$, $[d, 1, d]_{f=1}$, and $[d, 1, d]_{f=2}$ in terms of syndrome extraction rounds when (a, b, c) hardware-based or (d, e, f) sample-based syndrome graph is used. The logical error rate is shown as the function of the number of the data qubits ($d = 3, 5, 7, 9$) with different structures as follows: (a, d) The logical error rate of repetition codes with no flag qubit, (b, e) a single-flag qubit, and (c, f) double-flag qubits.

stable in the IBM machine for bit-flip or phase-flip errors.

In Ref. [32, 33], a hypergraph was constructed using the flag qubit information to correct errors. A promising direction for future research could be to explore the potential of the hypergraph in reducing the logical error rates in repetition codes with flag qubits. Moreover, increasing the number of flag qubits between the data and syndrome qubits is possible. Investigating how logical error rates vary with an increase in the number of flag qubits can be a simple experiment for assessing syndrome extraction circuits that employ long-range entanglement in situations where connectivity is limited.

Acknowledgements

This work was supported by the Basic Science Research Program through the National Research

Foundation of Korea (NRF) funded by the Ministry of Education, Science, and Technology (NRF2022R1F1A1064459), and the Creation of the Quantum Information Science RD Ecosystem (Grant No. 2022M3H3A106307411) through the National Research Foundation of Korea (NRF) funded by the Korean government (Ministry of Science and ICT).

Data availability

The datasets generated and analyzed for this study are available from the corresponding authors upon reasonable request.

-
- [1] Google Quantum AI. Exponential suppression of bit or phase errors with cyclic error correction. *Nature* 595, 383 (2021).
 - [2] Google Quantum AI. Suppressing quantum errors by scaling a surface code logical qubit. *Nature* 614, 676-681 (2023).
 - [3] Bluvstein D, Evered SJ, Geim AA, Li SH, Zhou H, Manovitz T, et al. Logical quantum processor based on reconfigurable atom arrays. *Nature*, 1-3 (2023).
 - [4] J, Preskill. Quantum Computing in the NISQ era and beyond. *Quantum* 2, 79 (2018).
 - [5] Steane, A. M. Error correcting codes in quantum theory.

- Phys. Rev. Lett. 77, 793-797 (1996).
- [6] Gottesman, D. Stabilizer Codes and Quantum Error Correction. PhD thesis, California Institute of Technology (1997).
- [7] Bravyi, S. B., Kitaev, A. Y. Quantum codes on a lattice with boundary. Preprint at <https://arxiv.org/abs/quant-ph/9811052> (1998).
- [8] Dennis, E., Kitaev, A., Landahl, A., Preskill, J. Topological quantum memory. *J. Math. Phys.* 43, 4452-4505 (2002).
- [9] Kitaev, A. Y. Fault-tolerant quantum computation by anyons. *Ann. Phys.* 303, 2-30 (2003).
- [10] Fowler, A. G., Mariantoni, M., Martinis, J. M., Cleland, A. N. Surface codes: towards practical large-scale quantum computation. *Phys. Rev. A* 86, 032324 (2012).
- [11] Terhal, B. M. Quantum error correction for quantum memories. *Rev. Mod. Phys.* 87, 307 (2015).
- [12] Bravyi, S., Kitaev, A. Universal quantum computation with ideal clifford gates and noisy ancillas. *Phys. Rev. A* 71, 022316 (2005).
- [13] DiVincenzo, D. P., Aliferis, P. Effective fault-tolerant quantum computation with slow measurements. *Phys. Rev. Lett.* 98, 020501 (2007).
- [14] Chamberland, C., Iyer, P., Poulin, D. Fault-tolerant quantum computing in the Pauli or Clifford frame with slow error diagnostics. *Quantum* 2, 43 (2018).
- [15] Kim, Y. et al. Evidence for the utility of quantum computing before fault tolerance. *Nature* 618, 500-505 (2023).
- [16] Hertzberg, J. B. et al. Laser-annealing josephson junctions for yielding scaled-up superconducting quantum processors. *npj Quantum Inf.* 7, 1 (2021).
- [17] Chao, R., Reichardt, B. W. Fault-tolerant quantum computation with few qubits. *npj Quantum Information* 4.1 (2018)
- [18] Chao, R., Reichardt, B. W. Quantum error correction with only two extra qubits. *Phys. Rev. Lett.* 121, 050502 (2018).
- [19] Chao, R., Reichardt, B. W. Flag fault-tolerant error correction for any stabilizer code. *PRX Quantum* 1, 010302 (2020).
- [20] Chamberland, C., Beverland, M. E. Flag fault-tolerant error correction with arbitrary distance codes. *Quantum* 2, 53 (2018).
- [21] Benito, César, et al. Comparative study of quantum error correction strategies for the heavy-hexagonal lattice. arXiv preprint arXiv:2402.02185 (2024).
- [22] Kim, Y., Kang, J., Kwon, Y. Design of quantum error correcting code for biased error on heavy-hexagon structure. *Quantum Information Processing*, 22(6), 230. (2023)
- [23] Gupta, Riddhi S., et al. Encoding a magic state with beyond break-even fidelity. *Nature* 625.7994, 259-263 (2024).
- [24] Andersen, Christian Kraglund, et al. Repeated quantum error detection in a surface code. *Nature Physics* 16.8, 875-880 (2020).
- [25] Egan, Laird, et al. Fault-tolerant control of an error-corrected qubit. *Nature* 598.7880, 281-286 (2021).
- [26] Ryan-Anderson, Ciaran, et al. Realization of real-time fault-tolerant quantum error correction. *Phys. Rev. X* 11.4, 041058 (2021).
- [27] Krinner, Sebastian, et al. Realizing repeated quantum error correction in a distance-three surface code. *Nature* 605.7911, 669-674 (2022).
- [28] Wootton, James R., and Daniel Loss. Repetition code of 15 qubits. *Physical Review A* 97.5: 052313 (2018).
- [29] Abobeih, M. H., et al. Fault-tolerant operation of a logical qubit in a diamond quantum processor. *Nature* 606.7916, 884-889 (2022).
- [30] Zhao, Youwei, et al. Realization of an error-correcting surface code with superconducting qubits. *Phys. Rev. Lett.* 129.3, 030501 (2022).
- [31] Gicev, S., Hollenberg, L. C., Usman, M. Quantum computer error structure probed by quantum error correction syndrome measurements. arXiv preprint arXiv:2310.12448 (2023).
- [32] Sundaresan, N., Yoder, T.J., Kim, Y. et al. Demonstrating multi-round subsystem quantum error correction using matching and maximum likelihood decoders. *Nat. Commun.* 14, 2852 (2023).
- [33] Chamberland, C., Zhu, G., Yoder, T. J., Hertzberg, J. B., Cross, A. W. Topological and subsystem codes on low-degree graphs with flag qubits. *Phys. Rev. X* 10, 011022 (2020)
- [34] Chen, E. H. et al. Calibrated decoders for experimental quantum error correction. *Phys. Rev. Lett.* 128, 110504 (2022).
- [35] IBM Quantum and Community. Qiskit: An open-source framework for quantum computing. <https://doi.org/10.5281/zenodo.2573505> (2021).
- [36] Ryan-Anderson, C. et al. Realization of real-time fault-tolerant quantum error correction. *Phys. Rev. X* 11, 041058 (2021).
- [37] O, Higgott PyMatching: A Python Package for Decoding Quantum Codes with Minimum-Weight Perfect Matching *ACM Transactions on Quantum Computing* 3.3 (2022)
- [38] O, Higgott, C, Gidney Sparse Blossom: correcting a million errors per core second with minimum-weight matching arXiv:2303.15933 (2023)
- [39] Gottesman, D. The Heisenberg representation of quantum computers. Preprint at <https://arxiv.org/abs/quant-ph/9807006> (1998).
- [40] Anders, S., Briegel, H. J. Fast simulation of stabilizer circuits using a graph-state representation. *Phys. Rev. A* 73, 022334 (2006).
- [41] Sundaresan, N. et al. Reducing Unitary and Spectator Errors in Cross Resonance with Optimized Rotary Echoes. *PRX Quantum* 1, 020318 (2020).
- [42] C, Gidney Stim: a fast stabilizer circuit simulator. *Quantum* 5, 497 (2021).
- [43] McKay, D. C., Wood, C. J., Sheldon, S., Chow, J. M., Gambetta, J. M. Efficient Z gates for quantum computing. *Phys. Rev. A* 96, 022330 (2017).
- [44] Magesan, E., Gambetta, J. M., Emerson, J. Characterizing quantum gates via randomized benchmarking. *Phys. Rev. A* 85, 042311 (2012).

T1(μ s)	T2(μ s)	Readout length(ns)
217.69	140.21	1400
1Q gate time(ns)		2Q gate time(ns)
60		660

Readout error	Idling error
1.90×10^{-2}	2.79×10^{-4}
1Q gate error	2Q gate error
2.79×10^{-4}	8.16×10^{-3}

TABLE III: Time and error information for the physical qubits in $[9, 1, 9]_{f=2}$. The table lists the average times of T1, T2, readout, single-qubit gates, and two-qubit gates.

The average error rates of readout, idling, single-qubit gates, and two-qubit gates are also displayed.

Supplementary information

A. Quantum hardware

1. Calibration table

Here, we describe the hardware specifications of `ibm_kyoto`. The hardware has a heavy-hexagon structure consisting of transmons of a fixed frequency. `ibm_kyoto` performs periodic calibrations in qubits and gates. Our study is based on the hardware specification at 2023-12-25-05:39:45 ~ 11:42:34 +00:00. Values can vary over time, even within the period. Table 3 displays a summary of the hardware specifications at the time when we run and obtain data for $|-\rangle_L$ in $[9, 1, 9]_{f=2}$.

The average values of time T1 and T2 of 49 physical qubits used are 217.69μ s and 140.21μ s, respectively. The longest operation among the hardware gates is the measurement, and its duration is 1400 ns. The 1Q gate is a single-qubit gate that contains X and \sqrt{X} except for R_Z, I . Because a virtual Z operation operates the R_Z gate, we do not physically apply the gate during the execution of the quantum circuits. The duration of the single-qubit gate is 60 ns. Meanwhile, the duration of the two-qubit gate (ECR) is 660 ns. The average error rate of 1Q gate is 2.79×10^{-4} . The I -gate error is an idling error, a decoherence error caused by the free evolution of a single qubit. The error rate of the 1Q gate is the same as that of the idling error.

2. ECR pulse

The 2Q gate denotes a two-qubit gate obtained by the ECR pulse. There are two ways to operate the ECR gate: 1. $\text{ECR01} = \frac{1}{\sqrt{2}}(IX - XY)$; 2. $\text{ECR10} = \frac{1}{\sqrt{2}}(XI - YX)$. When the CNOT pulse comprises an ECR pulse and single-qubit gates, the sequences of the gates differ according to ECR01 or ECR10. Fig. 13 depicts

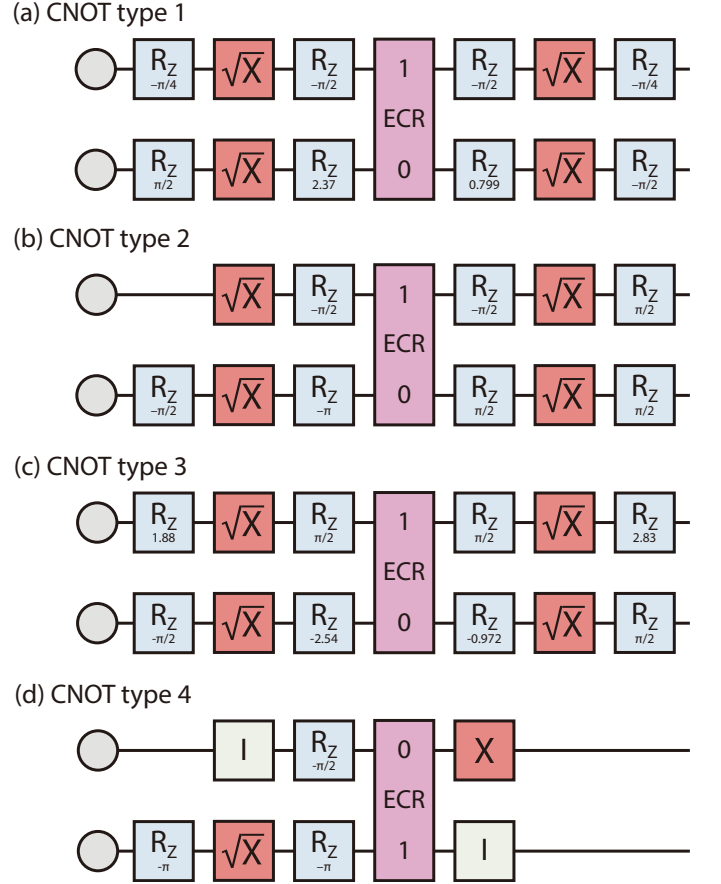


FIG. 13: Four different methods to implement the CNOT gate. The control and target qubits correspond to the upper and lower gray dots. The CNOT gate can be fragmented in four ways using the basis gate set from `ibm_kyoto`. The structure varies depending on what parameters are used in the R_Z gate and the type of the ECR gate.

the four cases created by combining the ECR pulse and single-qubit gates. The physical CNOT gate is designed to apply an X gate to one physical qubit, known as the target qubit, based on the state of another physical qubit, which serves as the control qubit. In the Figure, each case shows the CNOT gate designed to implement two physical qubits, grey dots, by choosing the top node as the control qubit and the bottom node as the target qubit. Since idling errors occur because free evolution occurs before and after the ECR pulse, the depth of the circuit is identical to those in the other cases. Therefore, the common feature of these four cases is that we require two single-qubit gates before and after the ECR pulse. We adopt these cases to construct a noisy CNOT gate for a hardware-based decoder. A CZ gate can also be constructed in many ways by choosing different gate sets, such as the type of ECR pulse and parameters for single-qubit gates. However, the depth of the gates in the CZ gate is identical to that in the CNOT gate, and both have

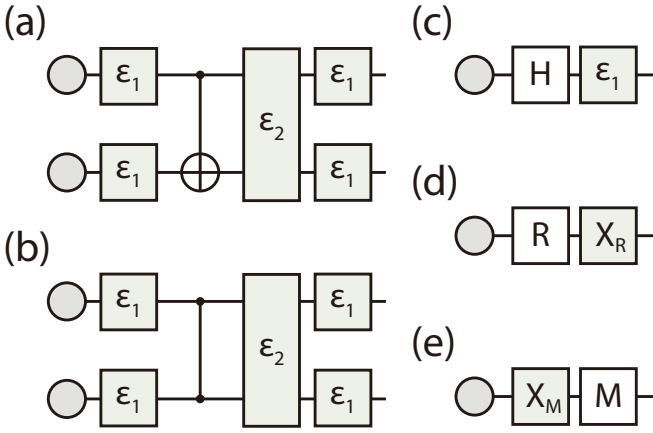


FIG. 14: Error model for five elements of a syndrome extraction circuit: (a) CNOT, (b) CZ, (c) Hadamard, (d) reset, and (e) measurement gate. ϵ_1 and ϵ_2 denote the depolarized error channels of single-qubit and two-qubit gates, respectively. X_R and X_M correspond to the X error for the reset and measurement gate. The error channel surrounds the ideal gate to construct the noisy one.

similar error channels. At the hardware level, these gate sequences can differ from what we apply physical pulses in a quantum circuit when optimizing them. However, we consider the logic gates where their noisy version is the worst case when modeling the error channel using its hardware calibration value.

3. Circuit-level noise model

Every gate of the repetition code consists of a Clifford gate. The depolarizing error channel for the gates can be constructed, as depicted in Fig. 14, based on the conversion from the basis gate of the real device. Fig. 14 (a), (b), (c), (d), and (e) depict the error models of the CNOT, CZ, Hadamard, reset, and measurement gates for constructing the hardware-based decoder with the Stim code. While X error channels are considered for reset and measurement gates, the depolarizing error channels are used for the other gates (CNOT, CZ, and H). We select the error rates for the error channels of the single and two qubits based on their gate error rate in the actual quantum device by considering the qubits where the gates were applied. We emphasize the consideration of depolarizing error channels on physical qubits when inactive during the execution of physical hardware. Each syndrome extraction circuit comprises nine steps, including syndrome and flag qubit measurement. Certain physical qubits do not undergo quantum gates during each step and experience free evolution, making them susceptible to errors. When designing the hardware-based syndrome graph, depolarizing error channels are accounted for considering their idling error rates from

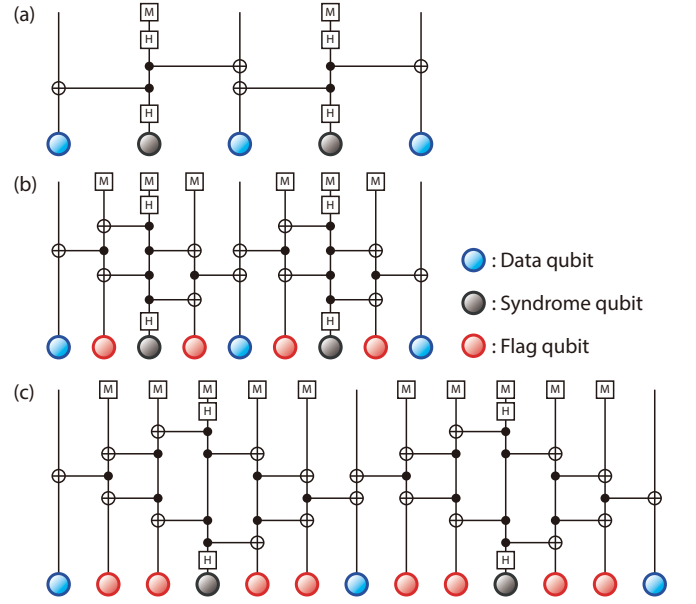


FIG. 15: Quantum circuits for the X syndrome extraction without and with flag qubits. The quantum circuits for the X syndrome extraction round are shown when there is (a) no flag qubit, (b) a single-flag qubit, and (c) double-flag qubits between a data qubit and a syndrome qubit.

the calibration table.

B. Repetition code on `ibm_kyoto`

1. X syndrome extraction circuit

The X syndrome extraction circuit detects the Z errors of the data qubits. Fig. 15 depicts the X syndrome extraction circuit for the structures without a flag qubit and with a single-flag qubit or double-flag qubits between the data and syndrome qubits. When flag qubits exist, the construction of the quantum circuit of the X syndrome extraction circuit is identical to that of the Z stabilizer, except when using the CNOT operator and not the CZ operator to interact with data and its neighbor flag qubit. Initialization errors on either flag or syndrome qubits can be detected in the same way as we have covered. However, the error that affects the state of a logical qubit is not an X error but a Z error. Since the code considers only Z errors and all data qubits are initialized on an X basis, the state of the logical qubit we are interested in is unaffected by X errors.

2. Selected qubit lists

We select the physical qubits for the double-flag qubit structure, as depicted in Fig. 16. When the logical qubit is initialized as $|-\rangle_L$, the average error rate for the error

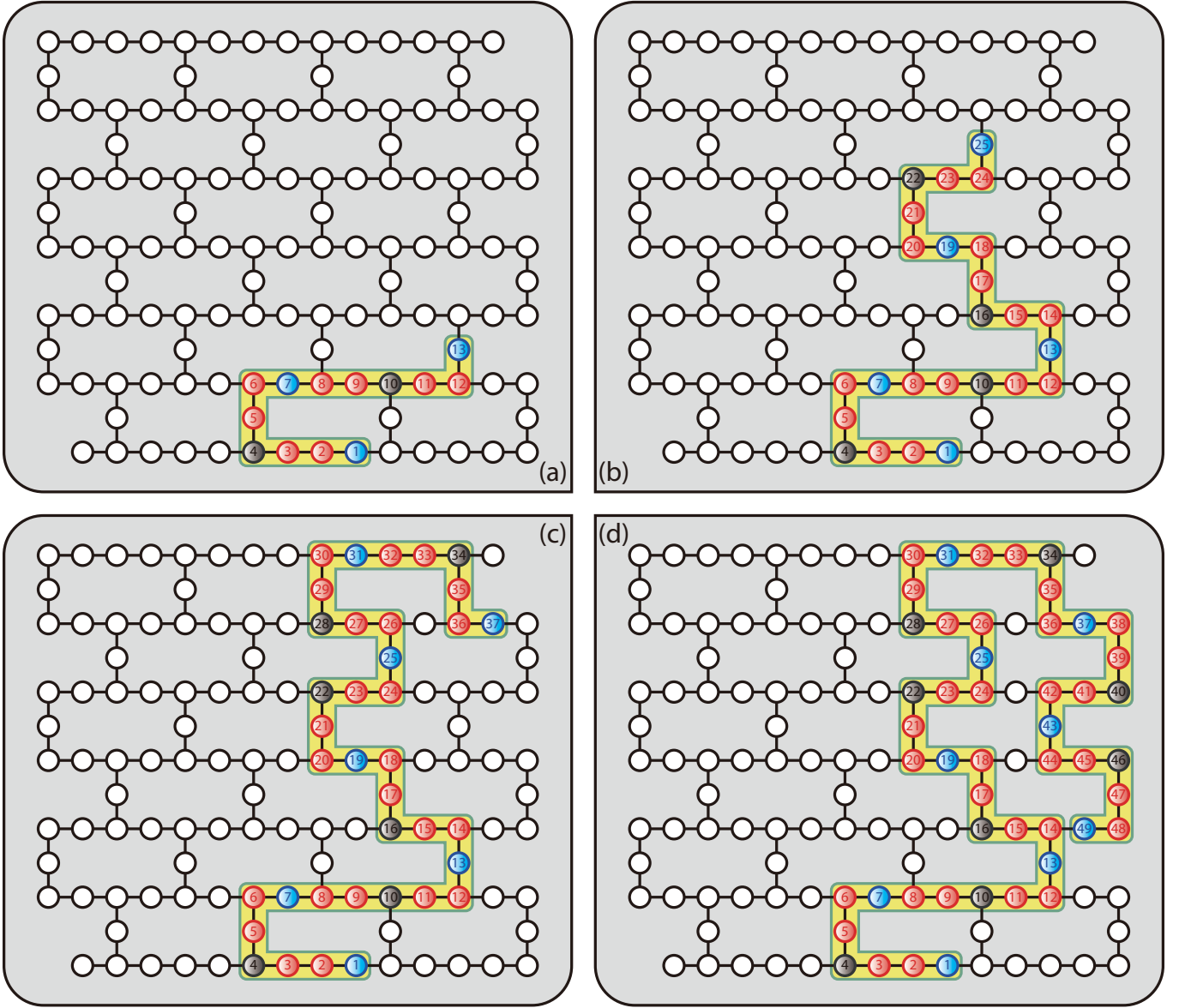


FIG. 16: Selected physical qubits for different distances $d = 3, 5, 7, 9$. The physical qubits that used in (a) $[3, 1, 3]_{f=2}$, (b) $[5, 1, 5]_{f=2}$, (c) $[7, 1, 7]_{f=2}$, and (d) $[9, 1, 9]_{f=2}$ are shown. The blue, red, and black dots correspond to data, flag, and syndrome qubits.

type for each case is as follows. The average readout error of $[3, 1, 3]_{f=0}([9, 1, 9]_{f=0})$ is $9.18 \times 10^{-3}(1.06 \times 10^{-2})$. The average readout error of $[3, 1, 3]_{f=1}([9, 1, 9]_{f=1})$ is $1.11 \times 10^{-2}(1.15 \times 10^{-2})$. Meanwhile, the average error rate of the ECR gate of $[3, 1, 3]_{f=0}([9, 1, 9]_{f=0})$ is $4.80 \times 10^{-3}(5.44 \times 10^{-3})$. The average error rate of the ECR gate of $[3, 1, 3]_{f=1}([9, 1, 9]_{f=1})$ is $5.91 \times 10^{-3}(6.61 \times 10^{-3})$. Fig. 17 depicts the qubits and error rates of gates when two flag qubits are introduced between a data qubit and a syndrome qubit. `ibm_kyoto` provides 127 qubits. Therefore, the qubit selection for the syndrome extraction circuit with flag qubits in the repetition code is not unique. We use the function “transpile” from the `qiskit` package to choose specific physical qubits that are

likely to provide the best performance among the possible combinations. In Fig. 18, the average error rates for each basis gate of the selected physical qubits in the hardware are plotted as a function of the distance and number of flag qubits between the data and syndrome qubits. As more flag qubits are added to the structure, the average error rates for all gates increase.

3. Syndrome calculation

Here, we explain the method used to obtain the syndromes from the outcomes of syndrome extraction circuits. When R round syndrome extraction is

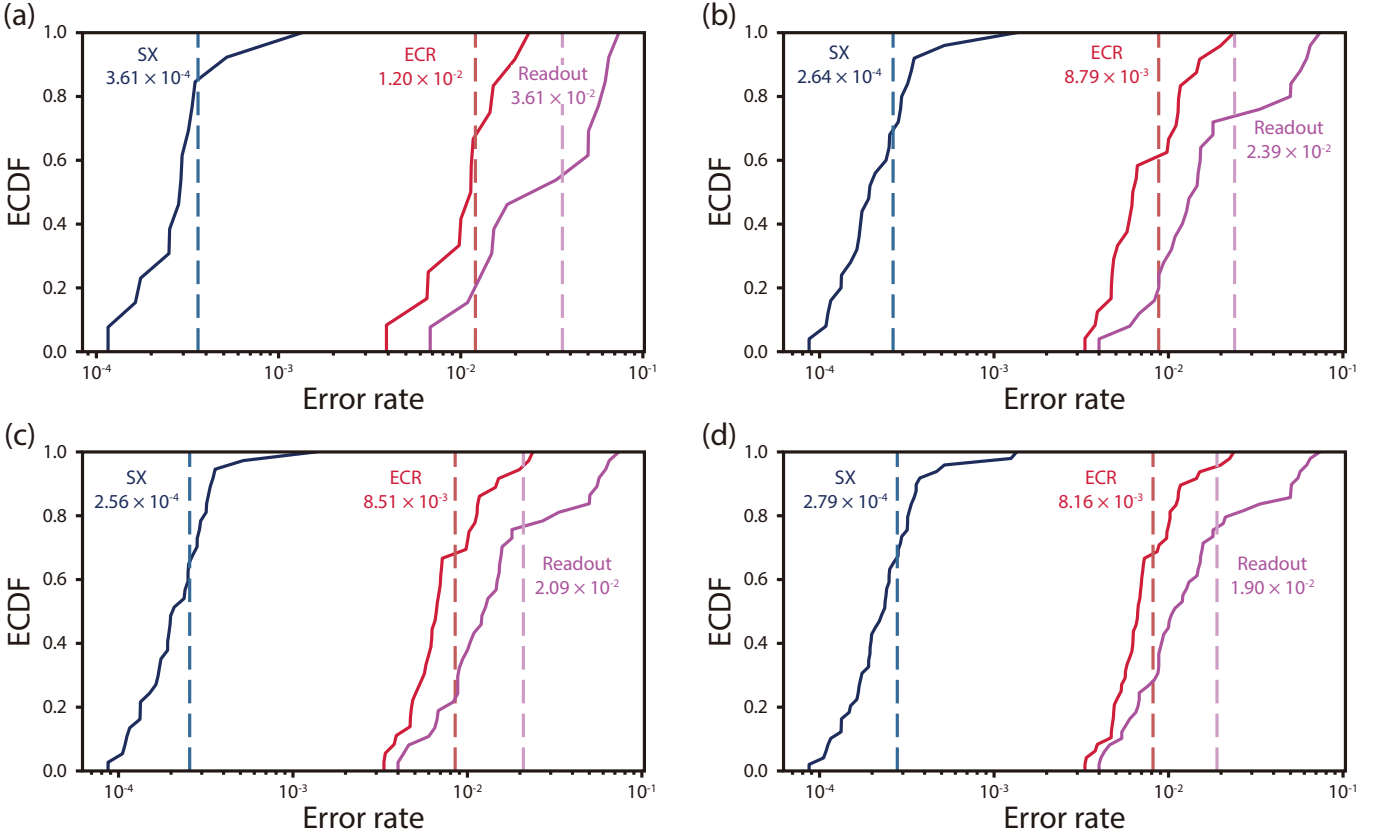


FIG. 17: Gate error rates of the physical qubits in the repetition codes with double-flag qubits. The figure shows the case of (a) $[3, 1, 3]_{f=2}$, (b) $[5, 1, 5]_{f=2}$, (c) $[7, 1, 7]_{f=2}$, and (d) $[9, 1, 9]_{f=2}$. The ECDF is plotted as the function of the error rates of the basis gate set of `ibm_kyoto` for each case.

performed, the syndrome can be broadly divided into three parts in terms of time T : 1. at $T = 0$, 2. from $T = 1$ to $T = (R - 1)$, and 3. at $T = R$. The method used to treat this syndrome is depicted in Fig. 19. The diagram depicts an example of a method for obtaining a syndrome with $[3, 1, 3]_{f=1}$ and $R = 3$. The initial data qubits are prepared with $|0\rangle_L = |000\rangle$. The outcomes from the syndrome extraction circuits can be divided into patches based on the syndrome qubits, and each patch is covered with red and black boxes containing three bits from the syndrome and flag qubits in Fig. 19. The calculation of a syndrome bit involves checking the parity of six values between two consecutive patches. The process is as follows: the system counts the number of occurrences of the digit ‘1’ among these six values. If the count is odd, the syndrome bit is set to ‘1’ otherwise, it is set to ‘0’. This method determines the syndrome bit based on the parity of observed values within a specified temporal range. For a syndrome bit located in the temporal boundary, two data qubits that are neighbors of a patch are used to calculate the syndrome bit. For instance, each syndrome bit in the initial syndrome round at $T = 0$ utilizes five bits comprising three values from the outcomes of the first round of a syndrome extraction circuit and two values from the initial states

of its adjacent data qubits. The process is the same for the syndrome bits in the final rounds ($T = 3$), except that the measured states of the data qubits are used instead of their initial states. The method for calculating the syndrome bit-string can be applied similarly to a structure involving double-flag qubits. The only variation lies in the specific number of bits, which is five in the case of double-flag qubits between the data and syndrome qubits within each patch.

4. Correlation matrix

The correlation matrix expresses the correlation between two syndrome nodes in a syndrome graph. Fig. 20 and 21 depict the correlation matrix obtained from 10 rounds of the X syndrome extraction circuit when $|-\rangle_L$ is prepared, and the number of samples is 50,000 in the case of double-flag qubits. The matrices are displayed with the space-time and time-space methods depicted in Fig. 20 and 21, respectively. The numbering in space-time is performed in terms of space, whereas that in time-space is processed in terms of time. Each pixel in the correlation matrix corresponds to an error probability, and the representation excludes negative

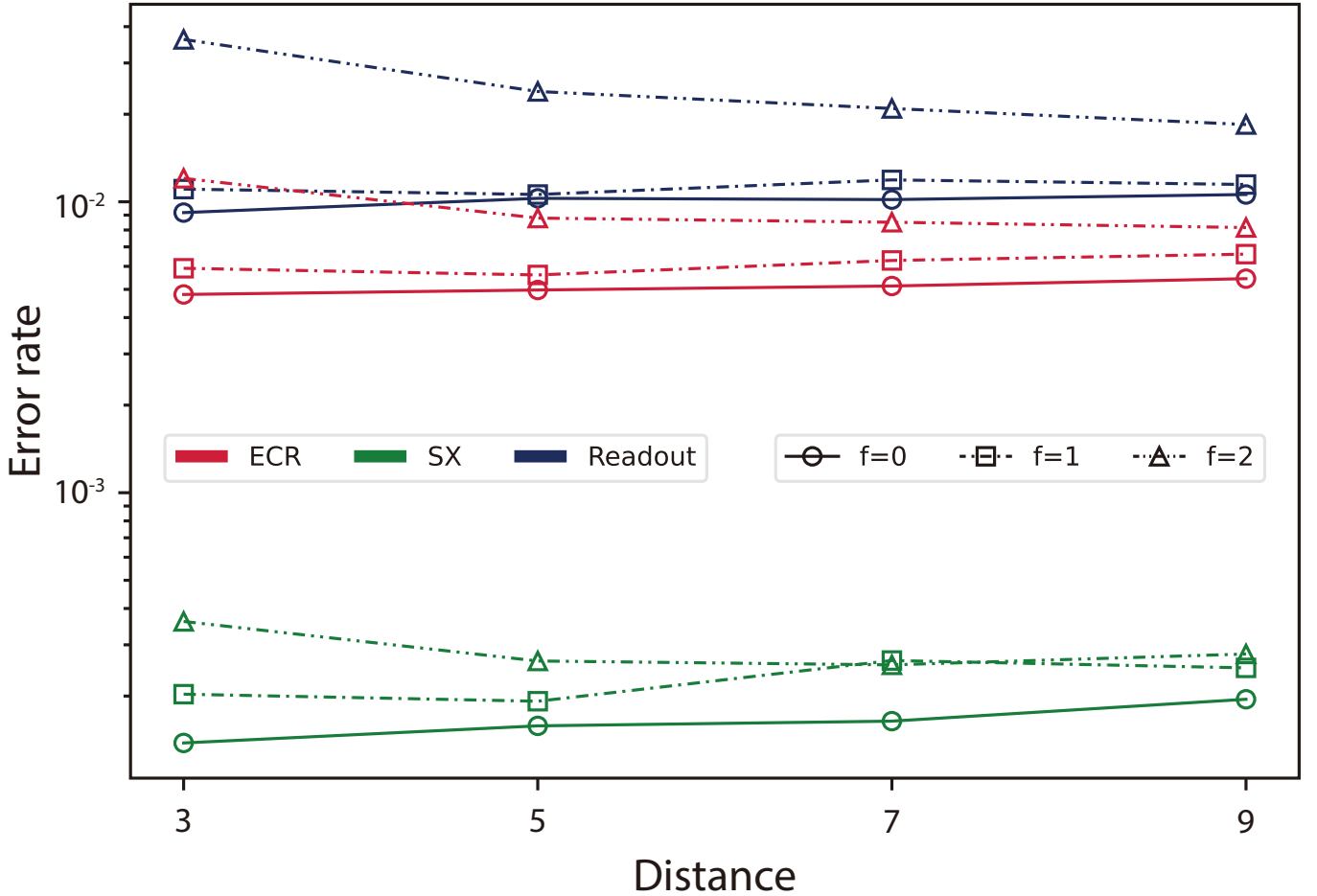


FIG. 18: Average error rates for each gate with different structures. The red, green, and blue markers represent the average error rate of ECR, single qubit gate, and readout, respectively. Meanwhile, the solid, dash-dotted, and dash double-dotted lines denote the structure with no flag qubit, a single-flag qubit, and double-flag qubits. As we add more flag qubits, the average error rates of the gates increase.

values. Moreover, the color scale is truncated to enhance visibility and clarity, with 0.2 as the maximum value. We emphasize positive error probabilities within the specified color scale while disregarding negative values to represent the error patterns accurately. The T errors are dominant for all cases, consistent with the hardware specifications.

In Ref [1], the cross-talk effects, observable in Time-Space correlation matrices, happen due to physical qubits locally nearby at the hardware level, even though they are not physically interacting in a quantum circuit. More specifically, the cross-talk effects can be seen from the correlation between syndrome bits that are spatially close in the real device but not neighbors in the perspective of the code. However, we are unable to observe these effects. In cases where we run the repetition code without flag qubits, this could be due to the initially selected physical qubits being locally separated at the hardware level. When flag qubits are employed in the syndrome extraction circuits, this lack of observation may be attributed to relatively high error rates resulting from including flag qubits in the structure, diminishing the

visibility of these effects.

5. Detection rate

The defect rate is defined as the ratio of the number of samples with detected syndromes to the total number of samples. Fig. 22 depicts the defect rate (gray line) from each syndrome qubit for $[9, 1, 9]_{f=2}$ versus the syndrome rounds. The red line represents the average of all defect rates for each syndrome qubits. The first (last) round also uses the initial (measured) state of the data qubits to identify the defect syndromes. Data are obtained by initializing the logical qubit as $|-\rangle_L$ with 50,000 samples. The number of syndrome extraction cycles is 10. Thus, there are 11 rounds of syndromes. We use data sampled from (a) `ibm_kyoto` and (b) the Stim code, which adopts the noise model of `ibm_kyoto`. Both cases have similar behavior regarding the probability of defect syndromes being lower in the first and last rounds than in other rounds and maintaining one value between them.

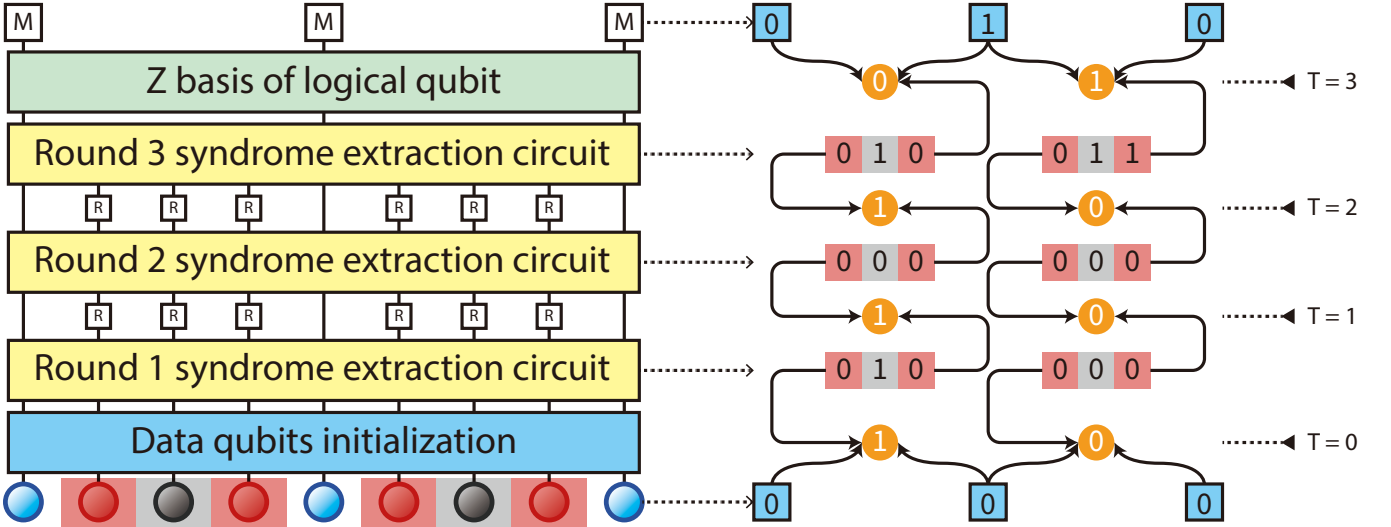


FIG. 19: Procedure for extracting the syndrome from the sampled data. The structure is $[3, 1, 3]_{f=1}$ and the number of the syndrome extraction circuit rounds is three. The initial logical qubit state is $|0\rangle_L$. Each syndrome extraction circuit produces six outcomes from the flag and syndrome qubits. Their outcomes can be grouped with red and black boxes. The syndrome bits corresponding to the orange dots can be calculated by checking the parity of two consecutive groups in temporal.

However, those values are not the same, which can be attributed to the oversimplification of each qubit's error channel as a depolarizing and idling error model. This suggests that the system on the device is more vulnerable to errors than we initially model.

6. Logical error rates

The logical error rates for each initial state are evident in Fig. 23. The Hardware-based decoder calculates the number of faults and corrected samples. To sample the data from `ibm_kyoto`, the experimental implementation is the same, except for the initial state of the logical qubit and syndrome extraction circuit based on the basis: 1. The Z basis logical qubit ($|1\rangle_L$) 2. X basis logical qubit ($|-\rangle_L$). The Z(X) basis logical qubit uses a syndrome extraction circuit constructed by the Z(X) stabilizers and considers only X(Z) errors in the system.

7. Samples

The sampled data are categorized into non-detected, corrected, and non-corrected. Non-detected samples are those in which the defect syndrome is not detected due to the absence of error. Corrected samples correspond to the data in which defect syndromes are detected and corrected; if these are not corrected, they belong to the non-corrected samples. In Fig. 24, the ratio of the categorized samples is shown with stacked bar charts for all cases of $[d, 1, d]_f$ for both the hardware- and sample-based decoders. Although the samples are non-

defective, a logical error can occur, which can be sorted as non-corrected instead of non-defective. As the structure size increases, the proportion of non-defects decreases. It is worth pointing out that most data samples are categorized as corrected samples as we increase the structure size.

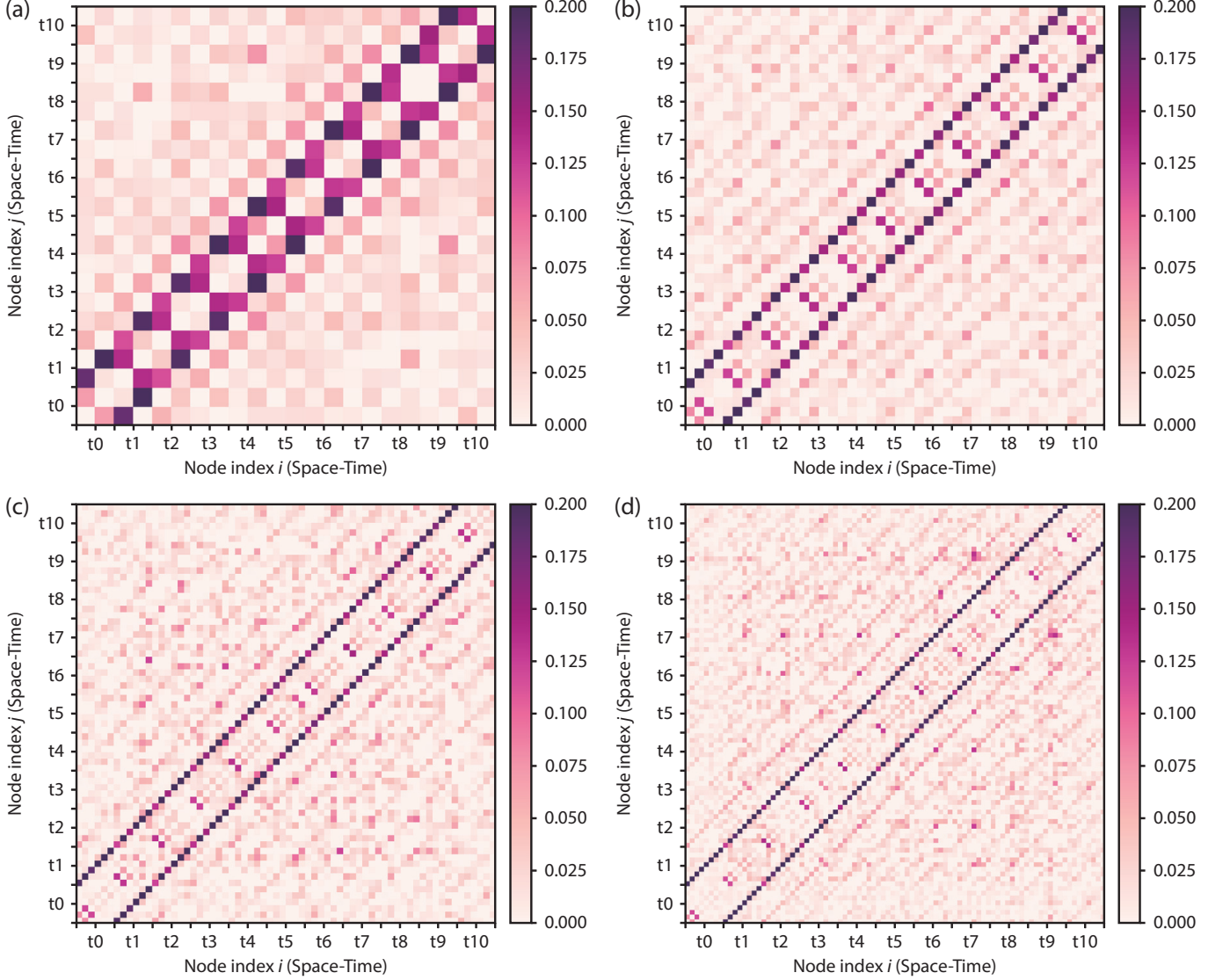


FIG. 20: Space-Time correlation matrices obtained in the structures with double-flag qubits. Space-Time correlation matrices are shown in the case of (a) $[3, 1, 3]_{f=2}$, (b) $[5, 1, 5]_{f=2}$, (c) $[7, 1, 7]_{f=2}$, and (d) $[9, 1, 9]_{f=2}$. The data is collected from the experiment with $|-\rangle_L$ state. Ten rounds of the syndrome extraction circuit are implemented. The number of samples is 50,000.

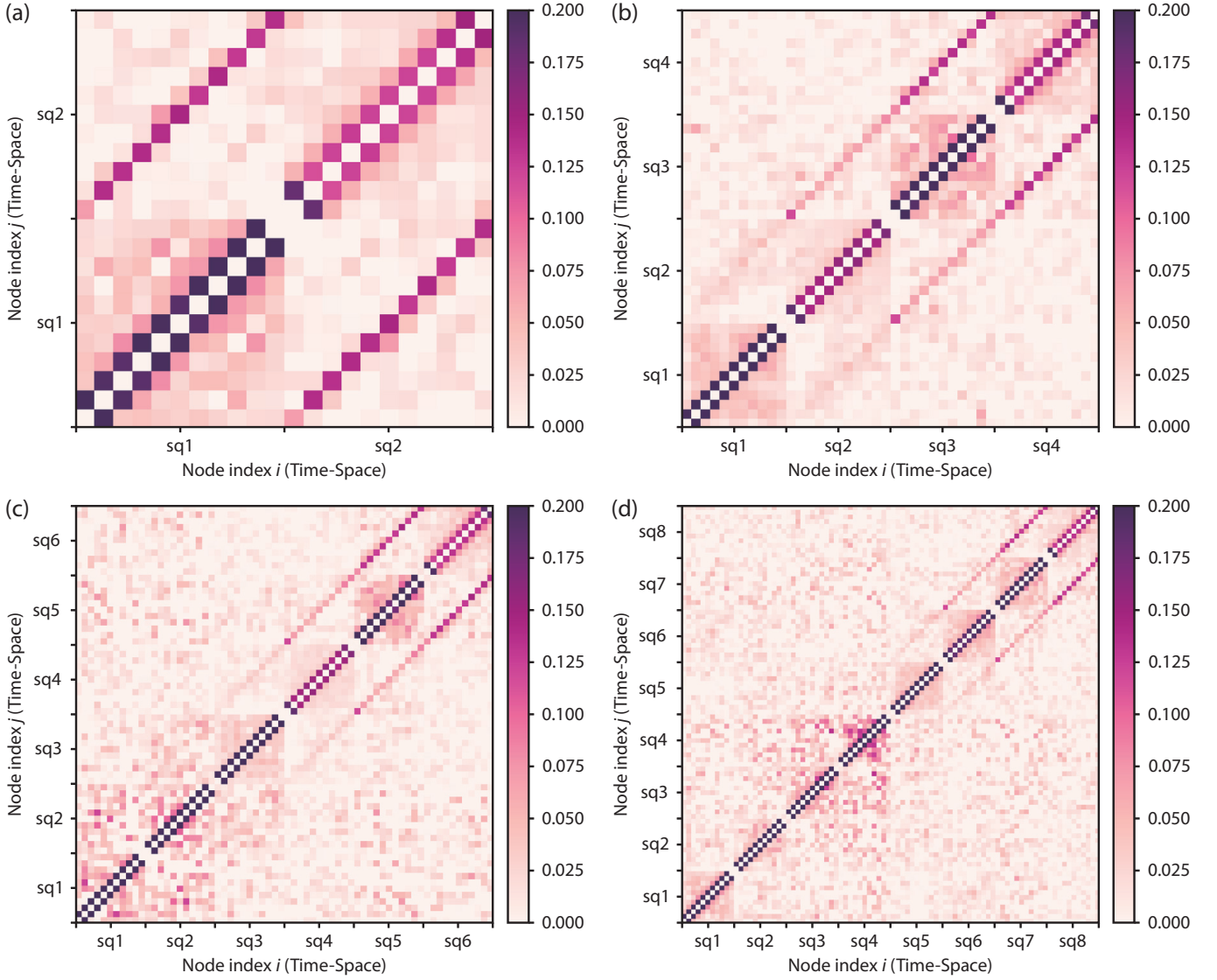


FIG. 21: Time-Space correlation matrices obtained in the structures with double-flag qubits. Time-Space correlation matrices are shown in the case of (a) $[3, 1, 3]_{f=2}$, (b) $[5, 1, 5]_{f=2}$, (c) $[7, 1, 7]_{f=2}$, and (d) $[9, 1, 9]_{f=2}$. The data is collected from the experiment with $|-\rangle_L$ state. Ten rounds of the syndrome extraction circuit are implemented. The number of samples is 50,000.

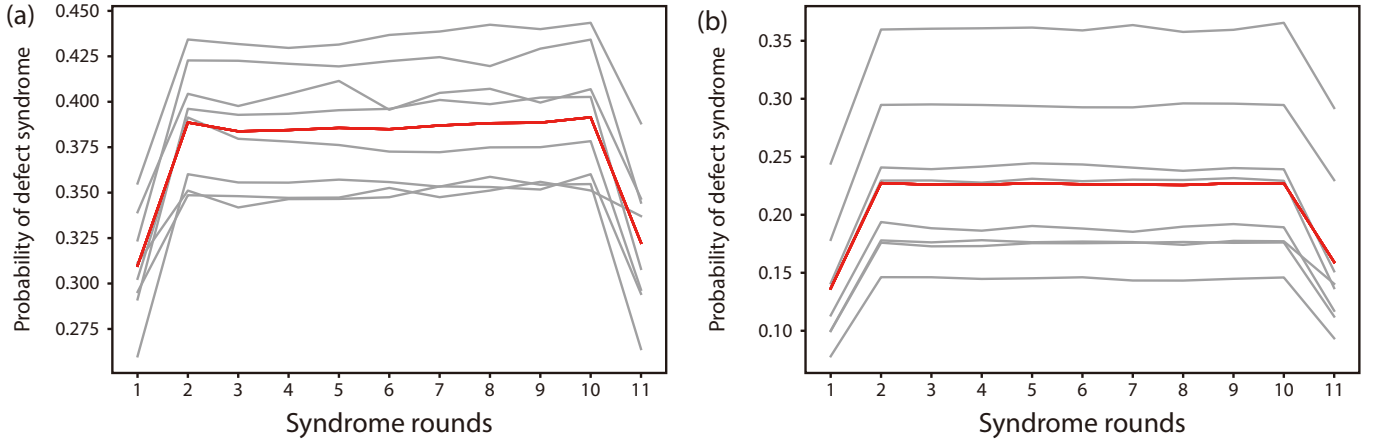


FIG. 22: The probability of defect syndromes. The probability of defect syndromes for the $|-\rangle_L$ state in the $[[9, 1, 9]]_{f=2}$ structure is shown in the case of (a) real quantum device, `ibm_kyoto`, and (b) Stim code. The data is collected from the experiment with $|-\rangle_L$ state. Here, the number of syndrome rounds is eleven. The number of samples is 50,000.

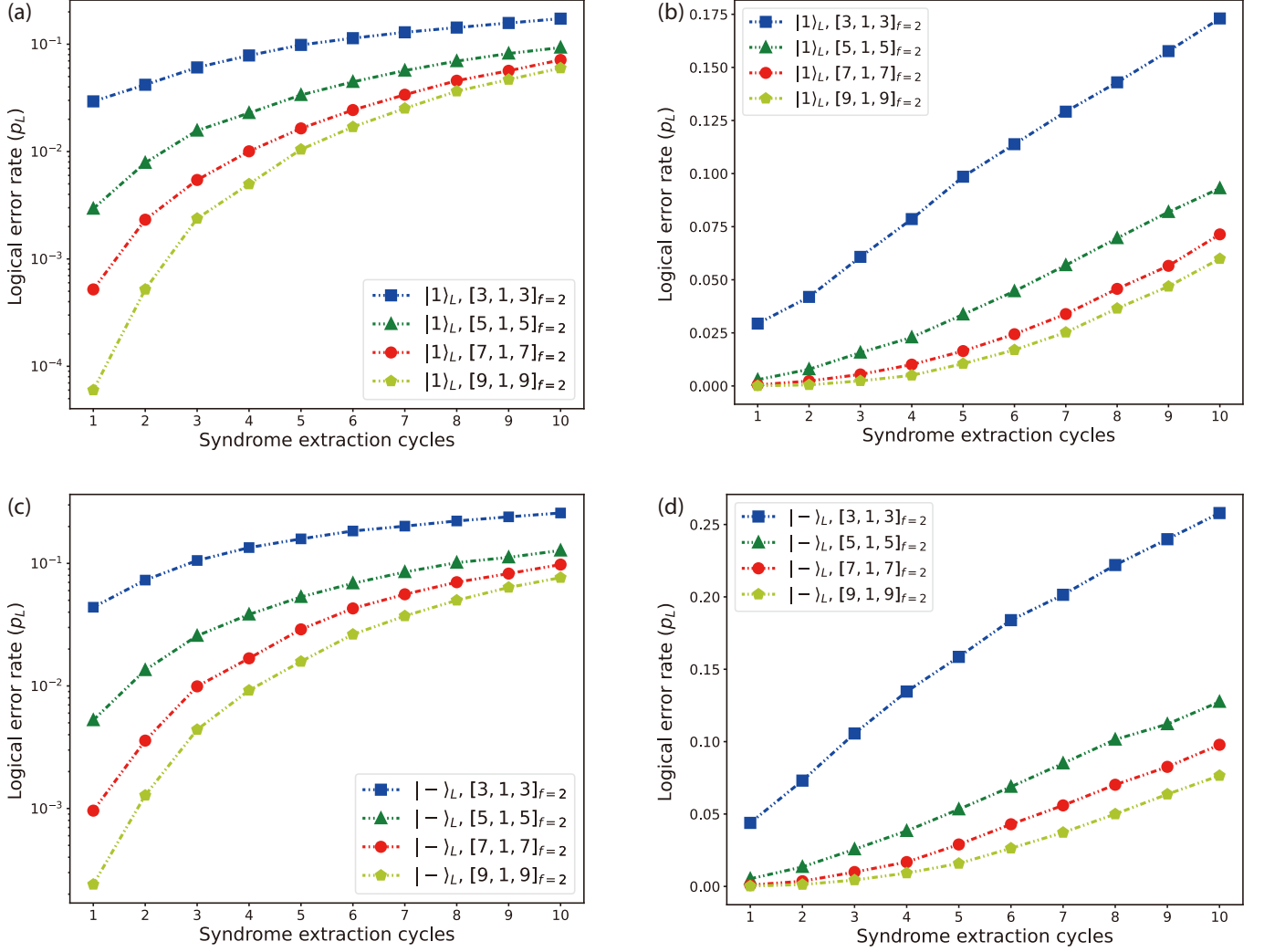


FIG. 23: Logical error rates for the structure with double-flag qubits and different initial logical states. The logical error rates in the case of $|1\rangle_L$ are plotted on (a) a log scale and (b) a linear scale for the vertical axis. Likewise, the logical error rates in the case of $|-\rangle_L$ are plotted on (c) a log scale and (d) a linear scale for the vertical axis. The logical error rates are obtained from the hardware-based decoder.

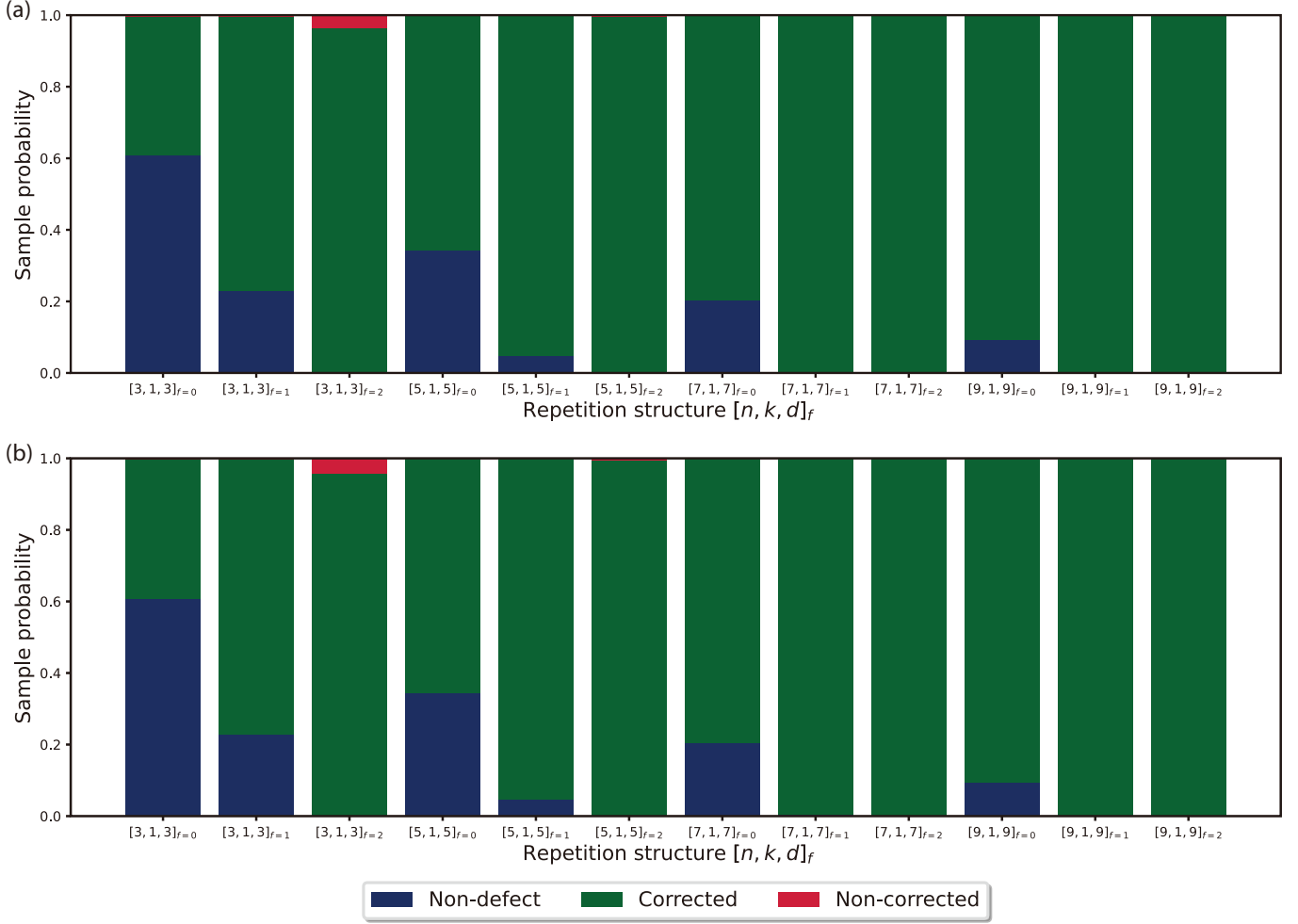


FIG. 24: The probability of the categorized results for all cases of repetition codes. The data from (a) the hardware-based and (b) sample-based decoder is categorized. The samples can be divided into three classes: non-defect (blue bar), corrected (green bar), and non-corrected (red bar). Each case with a different structure regarding the distance and the number of flag qubits is indicated using the stacked bars.